

Efficient Promoters and Reaction Paths in the CO₂ Hydrogenation to Light Olefins over Zirconia-Supported Iron Catalysts

Barrios, Alan J.; Peron, Deizi V.; Chakkingal, Anoop; Dugulan, Achim Iulian; Moldovan, Simona; Nakouri, Kalthoum; Thuriot-Roukos, Joëlle; Wojcieszak, Robert; Thybaut, Joris W.; More Authors

DOI

[10.1021/acscatal.1c05648](https://doi.org/10.1021/acscatal.1c05648)

Publication date

2022

Document Version

Final published version

Published in

ACS Catalysis

Citation (APA)

Barrios, A. J., Peron, D. V., Chakkingal, A., Dugulan, A. I., Moldovan, S., Nakouri, K., Thuriot-Roukos, J., Wojcieszak, R., Thybaut, J. W., & More Authors (2022). Efficient Promoters and Reaction Paths in the CO₂ Hydrogenation to Light Olefins over Zirconia-Supported Iron Catalysts. *ACS Catalysis*, 12(5), 3211-3225. <https://doi.org/10.1021/acscatal.1c05648>

Important note

To cite this publication, please use the final published version (if applicable).
Please check the document version above.

Copyright

Other than for strictly personal use, it is not permitted to download, forward or distribute the text or part of it, without the consent of the author(s) and/or copyright holder(s), unless the work is under an open content license such as Creative Commons.

Takedown policy

Please contact us and provide details if you believe this document breaches copyrights.
We will remove access to the work immediately and investigate your claim.

Efficient Promoters and Reaction Paths in the CO₂ Hydrogenation to Light Olefins over Zirconia-Supported Iron Catalysts

Alan J. Barrios, Deizi V. Peron, Anoop Chakkingal, Achim Iulian Dugulan, Simona Moldovan, Kalthoum Nakouri, Joëlle Thuriot-Roukos, Robert Wojcieszak, Joris W. Thybaut, Mirella Virginie, and Andrei Y. Khodakov*



Cite This: *ACS Catal.* 2022, 12, 3211–3225



Read Online

ACCESS |



Metrics & More



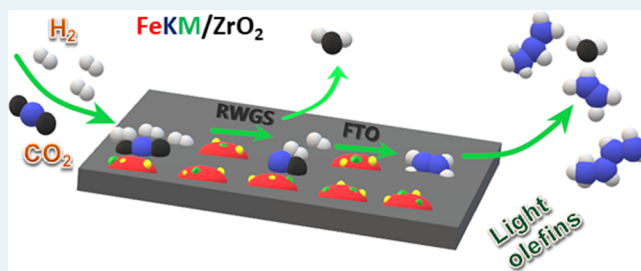
Article Recommendations



Supporting Information

ABSTRACT: Hydrogenation into light olefins is an attractive strategy for CO₂ fixation into chemicals. In this article, high throughput experimentation and extended characterization were employed to identify the most efficient promoters and to elucidate structure–performance correlations and reaction paths in the CO₂ hydrogenation to light olefins over zirconia-supported iron catalysts. K, Cs, Ba, Ce, Nb, Mo, Mn, Cu, Zn, Ga, In, Sn, Sb, Bi, and V were added in the same molar concentrations to zirconia-supported iron catalyst and evaluated as promoters. The CO₂ hydrogenation proceeds via intermediate formation of CO followed by surface polymerization. Over the iron catalysts containing alkaline promoters, initially higher selectivity to light olefins shows a significant decrease with the CO₂ conversion, because of further surface polymerization and the formation of longer chain hydrocarbons. A relatively low selectivity to light olefins over the promoted catalysts, without potassium, is not much affected by the CO₂ conversion. Essential characteristics of iron catalysts to obtain a higher yield of light olefins seem to be a higher iron dispersion, a higher extent of carburization, and optimized basicity. The strongest promoting effect is reported for the alkaline metals. A further increase in the light olefin selectivity is observed after simultaneous addition of potassium with copper, molybdenum, gallium, or cerium.

KEYWORDS: CO₂ mitigation, hydrogenation, light olefins, iron catalysts, high throughput



1. INTRODUCTION

The growing concentration of CO₂ in the atmosphere is the major reason for climate change. There are currently two strategies for dealing with the ever-increasing levels of CO₂: carbon capture and storage (CCS)¹ and carbon capture and utilization (CCU).² CCS is based on the capture of CO₂ from power plants and industrial facilities including its separation, compression, and transport, for permanent storage in a geological layer. CCU involves either direct technological use of CO₂ or its chemical and biological conversion into high value-added products.^{2–4}

The CO₂ fixation into chemicals is an essential CCU strategy. In this strategy, CO₂ can be considered not only the major pollutant but also a feedstock for the synthesis of valuable chemicals and fuels.^{5,6} Nevertheless, CO₂ chemical utilization is challenging, because of its thermodynamic stability, resulting in low conversion.⁷ With sustainable hydrogen as the co-reagent, CO₂ can be hydrogenated⁷ to methanol,^{8–10} dimethyl ether,^{11–14} formic acid,^{15,16} higher alcohols,¹⁷ liquid hydrocarbon fuels,^{18,19} aromatics,²⁰ and light olefins.^{7,21–24} The light olefin synthesis from CO₂ has attracted particular attention in recent years from both academia and companies, because ethylene, propylene, and butylenes are

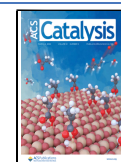
major building blocks in the chemical industry. These compounds are widely used in manufacturing polymers, chemical intermediates, and solvents. Currently, light olefins are mainly produced by steam cracking²⁵ of light hydrocarbon fractions, FCC,²⁶ dehydrogenation of light alkanes,²⁷ and the methanol to olefins (MTO) process.^{28–30} Recently, novel bifunctional or multifunctional catalysts, which are composed of metal oxide nanoparticles and zeolites, have been proposed^{22,31–33} for the hydrogenation of CO₂ into light olefins via the so-called “methanol-mediated route”. A lower catalytic activity, a higher selectivity to coproduced CO (>60–80%), and an insufficient olefin yield (usually less than 7%^{32,33}) represent major drawbacks of this approach.

The CO₂ Fischer–Tropsch (CO₂-FT) synthesis, which allows one to achieve a higher single-pass yield, is a promising

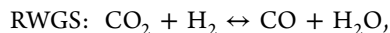
Received: December 8, 2021

Revised: February 10, 2022

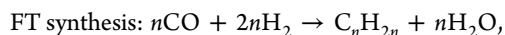
Published: February 23, 2022



route to transform CO₂ into light olefins.³⁴ The CO₂ conversion into olefins proceeds via a combination of the reverse water gas shift reaction (RWGS) and the Fischer–Tropsch (FT) synthesis:



$$\Delta_{\text{R}}H_{300^\circ\text{C}} = +38 \text{ kJ/mol}$$



$$\Delta_{\text{R}}H_{300^\circ\text{C}} = -165 \text{ kJ/mol}$$

Because of their high activity in both RWGS and FT reactions, iron-based catalysts remain the principal option for the CO₂-FT synthesis. Nonetheless, iron employment by itself does not necessarily result in a sufficiently high light olefin selectivity. The optimization of catalyst chemical composition and structure is therefore required to attain high and selective yield of these products. Most commonly, iron catalysts for CO₂ hydrogenation to light olefins have been supported by oxides or carbon materials. In particular, SiO₂, TiO₂, Al₂O₃, ZrO₂, and carbon materials have been evaluated³⁵ as supports. Strong hydrophilicity and instability of the alumina support could be detrimental for the CO₂ hydrogenation, which generates larger amounts of water than does the CO hydrogenation. Relatively weak hydrophilic character of the support could be one of the required characteristics for the CO₂ hydrogenation catalysts. Among the investigated supports, the ZrO₂-supported catalysts have shown the highest selectivity and yield of light olefins.³⁵ Recent results suggest^{36,37} that higher selectivity to light olefins can be achieved using carbon materials as supports of iron catalysts. Note, however, that the stability of carbon-based catalysts can be a problem for industrial applications, because the activation and regeneration of the catalysts usually involve oxidative treatments with air.

The iron CO₂-FT catalysts are most commonly promoted with potassium,^{35,38–47} Co,^{48–52} Cu,^{53,54} Mn,^{46,47,55} and/or Zn.^{32,45,56,57} Much less information is available on the promotion with other elements. Note that unambiguous identification of the most efficient promoters for iron CO₂ hydrogenation catalysts seems challenging. First, the iron catalysts prepared and investigated by different research groups may have different contents of promoters. Second, different catalyst activation and reaction procedures even with the same catalyst employed by different groups may lead to different catalytic performance. In this work, we used three groups of promoters for zirconia-supported iron catalysts. First, we selected alkali metals, which bring strong basicity.^{58,59} Second, we promoted iron catalysts with transition metals, which can have multiple oxidation states favoring carbon dioxide activation. Finally, “soldering” metals^{60,61} like Bi, Sn, and Sb were used for the promotion. They have a low melting point that could give them higher mobility⁶² on the catalyst surface.

High-throughput experimentation (HTE)^{63–66} is a fast, reliable, and powerful technique generating a tremendous amount of data and is effective for discovering new catalysts. Recently, the HTE strategy⁶⁷ uncovered novel highly efficient promoters such as “soldering metals” (Bi, Pb, Sn, and Sb) for high-temperature FT synthesis with syngas over iron catalysts.

This article focuses, on the one hand, on the selection of the most efficient new promoters for iron catalysts, on the identification of structure–performance correlations, and, on the other hand, on the elucidation of reaction paths in CO₂

hydrogenation over promoted iron catalysts. The promoters were added in the same molar concentrations; the catalysts were activated and tested under the same conditions. The effects of 15 different elements (K, Cs, Ba, Ce, Nb, Mo, Mn, Cu, Zn, Ga, In, Sn, Sb, Bi, and V) on the Fe/ZrO₂ catalyst structure and CO₂ hydrogenation to light olefins were investigated over zirconia-supported iron catalysts using HTE catalytic measurements and a large combination of characterization techniques: XRF, nitrogen adsorption, XRD, TPR, TPD, TGA/DSC, in situ Mössbauer spectrometry, STEM-HAADF, and STEM-EDS.

2. EXPERIMENTAL SECTION

2.1. Catalyst Preparation. Commercial zirconia (Alpha Aesar) was used as the catalytic support. Distilled water was used as solvent. In the case of Nb, Sn, and Sb salts, ethanol (Verbiede) was used as a solvent, because of the insolubility of those salts in water. The following precursors were used for the promotion of zirconia-supported iron catalysts: KNO₃ (Sigma-Aldrich), CsNO₃ (Sigma-Aldrich), Ba(NO₃)₂ (Sigma-Aldrich), Ce(NO₃)₃·6H₂O (Fluka), NbCl₅ (Alfa Aesar), (NH₄)₆Mo₇O₂₄·4H₂O (Sigma-Aldrich), Mn(NO₃)₂·4H₂O (Sigma-Aldrich), Cu(NO₃)₂·3H₂O (Acros Organics), Zn(NO₃)₂·6H₂O (Sigma-Aldrich), Ga(NO₃)₃·xH₂O (Sigma-Aldrich), In(NO₃)₃·xH₂O (Sigma-Aldrich), SnCl₄·2H₂O (Sigma-Aldrich), SbCl₃ (Sigma-Aldrich), Bi(NO₃)₃·5H₂O (Sigma-Aldrich), and NH₄VO₃ (Sigma-Aldrich).

Apart from the Sb-promoted iron catalyst, all of the other promoted catalysts were synthesized by the single-step coimpregnation method. During the coimpregnation, the precursors of potassium and the second promoter were added at the same time. In the case of Sb promoted catalysts, we introduced first Sb and then potassium. A 0.2 M solution of Fe(NO₃)₃·9H₂O along with the promoter salt was added dropwise to the zirconia support. The concentrations of the impregnating solutions were calculated to obtain about 10 wt % iron in the final catalysts; the atomic ratio of Fe to promoter (M) was 50:1. The nominal concentration of potassium in the catalysts was 1 wt %. After the impregnating solution was added to ZrO₂, the mixture was stirred for 8 h at room temperature. Next, the solvent was evaporated at 80 °C. The catalysts then were dried overnight in an oven at 120 °C. Finally, they were calcined in air at 500 °C for 5 h with a 1 °C/min temperature ramp. Two different sets of catalysts without and with potassium denominated, respectively, as FeM/ZrO₂ and FeKM/ZrO₂ were synthesized, where M represents Cs, Ba, Ce, Nb, Mo, Mn, Cu, Zn, Ga, In, Sn, Sb, Bi, or V. The chlorine contents in the catalysts prepared using chlorine-containing precursors (SbCl₃ and NbCl₅) were measured by FRX. The chlorine contents were relatively low (0.007 wt %) in FeSb/ZrO₂ and 0.63 wt % in FeNb/ZrO₂.

2.2. Catalyst Characterization. The low-temperature N₂ physisorption measurements were carried out on a Micromeritics Tristar II PLUS Surface Area and Porosimetry analyzer. The samples were degassed under vacuum at 120 °C for 3 h. The nitrogen adsorption–desorption isotherms were measured at −196 °C. The specific surface area of the samples was calculated by the BET method.

The relative promoter content was determined using an energy dispersive micro-X-ray fluorescence spectrometer M4 TORNADO (Bruker). The sample irradiation was made using a rhodium X-ray tube (50 kV/200 mA, 10 W). This X-ray source is equipped with a polycapillary lens enabling excitation

of an area of 200 μm . For each sample, 36 points (of 200 μm) were analyzed covering the entire sample surface. The detector used was a silicon-drift-detector Si(Li) with <145 eV resolution at 100 000 cps (Mn $K\alpha$) and cooled with Peltier cooling ($-20\text{ }^{\circ}\text{C}$). The measurement was done under vacuum (20 mbar). Quantitative analysis was done using fundamental parameters (FP) (standardless). The quantification was made on the basis of the identified element.

For the CO_2 temperature-programmed desorption (TPD) experiments, the samples were pretreated at $500\text{ }^{\circ}\text{C}$ in He for 1 h, cooled to $40\text{ }^{\circ}\text{C}$, and exposed to CO_2 for 30 min. The samples then were heated with the ramping rate of $10\text{ }^{\circ}\text{C}/\text{min}$ to reach $700\text{ }^{\circ}\text{C}$ in He flow. The CO_2 desorption was measured with a TCD detector.

The reduction behavior of the catalysts was evaluated by hydrogen temperature-programmed reduction (TPR) using an AutoChem II 2920 apparatus (Micromeritics). The samples ($\sim 0.05\text{ g}$) were reduced in a flow of 5% H_2/Ar flow (50 mL/min) and heated to $1000\text{ }^{\circ}\text{C}$ with the temperature ramp rate of $10\text{ }^{\circ}\text{C}/\text{min}$.

The samples were characterized by X-ray powder diffraction (XRD) using a Bruker AXS D8 diffractometer with monochromatic Cu $K\alpha$ radiation ($\lambda = 0.1538\text{ nm}$). The XRD patterns were collected with the 2θ range between 10° and 90° , using a step size of 0.02° and with an acquisition time of 0.5 s. The identification of crystalline phases present in the catalysts was carried out by comparison with the JCPDS standard software.

To determine the carbon deposition on the catalysts, the thermogravimetric analysis was performed using an SDT Q600 V20.9 Build 20 Thermogravimetric Analyzer (TGA) and a differential scanning calorimeter (DSC) with $\sim 10\text{ mg}$ of sample, with a temperature ramp of $5\text{ }^{\circ}\text{C}/\text{min}$ up to $600\text{ }^{\circ}\text{C}$ under air.

The catalysts activated in a flow of CO at $350\text{ }^{\circ}\text{C}$ and then passivated in a flow of nitrogen at room temperature were characterized using scanning transmission electron microscopy (STEM), under the high-angle annular dark-field imaging (STEM-HAADF) and energy-dispersive X-ray spectroscopy (STEM-EDS) modes. The powder specimens were dispersed in ethanol by ultrasounds, and a drop of suspension was deposited on a holey carbon film previously deposited on a 300 mesh TEM Cu grid. The catalysts were analyzed using STEM with a high energy beam of 200 kV and a beam size of $<1\text{ \AA}$ for the imaging purposes, whereas the chemical maps were carried out by a probe with a diameter of about 1 \AA . STEM-HAADF with Z-contrast enabled the identification of atoms and atom agglomerations of species associated with heavy elements. More specific, the heavier is the element, the higher is the contrast. The STEM-EDS mapping allowed the analysis of elemental composition within the samples. The analytical TEM Jeol-ARM200 cold FEG microscope with objective and probe correctors was used for these investigations. The STEM-EDS maps were acquired on a Jeol Centurio 100 mm^2 detector mounted on the TEM. A scanning speed of $20\text{ }\mu\text{s}/\text{px}$ was employed for imaging within the Digital Micrograph software and $0.05\text{ }\mu\text{s}/\text{px}$ for STEM-EDS elemental mapping using the Analysis Station software, respectively. The map size was fixed at $256 \times 256\text{ px}$ with a spatial drift correction every 60 s. To gather maps with high signal-to-noise ratios, chemical mapping was carried out for durations between 80 and 180 min. The elemental maps were used in a first approach to assess qualitatively the presence, distribution, and location of the

elements of interest and to quantitatively estimate the size of the Fe nanoparticles, in a second time. The size distribution histogram of each sample was conducted on the basis of more than 100 nanoparticles taken from different micrographs acquired in the Digital Micrograph software, while the elemental maps acquired in the Analysis Station were employed to assess for the size of the Fe nanoparticles (measured in the longer direction).

The transmission ^{57}Fe Mössbauer spectra were collected at $-153\text{ }^{\circ}\text{C}$ with a sinusoidal velocity spectrometer using a $^{57}\text{Co}(\text{Rh})$ source. The velocity calibration was carried out using an $\alpha\text{-Fe}$ foil at room temperature. The source and absorbing samples were kept at the same temperature during the measurements. The Mössbauer spectra were fitted using the Mosswin 4.0 program.⁶⁸ The experiments were performed at pressures up to 10 bar, in a state-of-the-art high-pressure Mössbauer in situ cell, which was recently developed at the Reactor Institute of Delft.⁶⁹ The high-pressure beryllium windows used in this cell contain 0.08% Fe impurity, whose spectral contribution was fitted and removed from the final spectra.

2.3. Catalytic Tests. The catalytic screening tests were performed both in the high throughput experimentation unit (HTE, Flowrence, Avantium) and in the laboratory fixed bed reactor. Further information about the HTE unit is available in ref 66. In the HTE unit, the feed gas is homogeneously split via previously calibrated high pressure-drop capillaries into 16 reactors. One of them filled with the inert support serves as the reference. Each of the four reactors forms an independent block, maintained at the same temperature. Any liquid phase (if produced) can be collected at $60\text{ }^{\circ}\text{C}$, while the remaining gas was subsequently sampled online for GC analysis. The catalysts were loaded in a stainless-steel tube with an inner diameter of 2.0 mm and a length of 15 cm. Both ends (height of 3.5 cm) of the reactor tube were filled with inert SiC (size of 105 and 210 μm), where the catalyst (grain size: 50–100 μm) was loaded in between. Prior to the CO_2 hydrogenation reaction, all catalysts were activated in CO (10 mL/min) under atmospheric pressure at $350\text{ }^{\circ}\text{C}$ for 10 h and cooled to $180\text{ }^{\circ}\text{C}$. At this temperature, the system was pressurized in H_2/CO_2 (3:1) to 10 bar, while the temperature was step-wisely ($1\text{ }^{\circ}\text{C}/\text{min}$) increased to $350\text{ }^{\circ}\text{C}$. The catalytic performance was measured under different WHSV values (4.67–18.19 L/g·h) staying for at least 12 h at each space velocity. The gaseous products were analyzed online using gas chromatography (GC). Permanent gases (He , H_2 , O_2 , N_2 , CH_4 , and CO) were separated by a Hayesep Q/Molecular Sieve column and determined by a thermal conductivity detector (TCD). CO_2 and $\text{C}_2\text{--C}_4$ hydrocarbons were separated and measured by a PPQ/PPQ column and TCD, while the $\text{C}_5\text{--C}_{12}$ hydrocarbons were separated by a CP-Sil5/CP-Sil5 column and a flame ionization detector (FID), respectively. The HTE unit is equipped with a 16 ways-valve system that allows the injection of the gases coming from each reactor one by one in a sequence mode. Also, the program used for gas analysis with GC was optimized and lasts a total of 12 min. The conversion and selectivity calculations are given in the [Supporting Information](#). The carbon balance was better than 92%.

In addition to HTE tests, the catalytic behavior of several promoted ZrO_2 -supported iron catalysts was also measured in the laboratory fixed-bed reactor with a 2 mm internal diameter and length of 15 cm. Both ends of the reactor tube were filled with inert SiC (size of 500 μm), where $\sim 110\text{ mg}$ of fresh

catalyst (grain size: 50–100 μm) had been loaded into the reactor. The catalysts were activated in CO under atmospheric pressure with a heating ramp of 2 $^{\circ}\text{C}/\text{min}$ until reaching the reaction temperature of 350 $^{\circ}\text{C}$ and dwelling at that temperature for 10 h under CO flow (10 mL/min). After the catalysts were cooled to 180 $^{\circ}\text{C}$, a gas mixture composed of $\text{H}_2/\text{CO}_2 = 3$ was fed into the reactor. Nitrogen with a flow of 1 cm^3/min was used as internal standard for the calculation of CO_2 conversion. After the flow rates and the pressure have been stabilized, the temperature was increased to 350 $^{\circ}\text{C}$ with a heating ramp of 1 $^{\circ}\text{C}/\text{min}$ to start the reaction. For the analysis of reagents and reaction products, a Varian CP-3800 chromatograph equipped with a TCD and an FID detector was used. Two columns were used for this analysis: the first is a packed CTR-1 column connected to the TCD detector, and the second is an Rt-Q-PLOT capillary column connected to the FID detector. There was no production of a liquid phase.

Iron time yields (FTY) were expressed as moles of CO_2 converted per gram of iron (determined from XRF) per second. The turnover frequency (TOF) values were calculated⁷⁰ using the density of Hägg iron carbide Fe_5C_2 ($\rho = 7.57 \text{ g}/\text{cm}^3$) and assuming 14 Fe atoms/ nm^2 . The CO-free hydrocarbon selectivities on carbon basis were calculated taking into account only hydrocarbon production in the CO_2 hydrogenation.

3. RESULTS

3.1. HTE Evaluation of the Promoted Iron Catalysts.

3.1.1. Catalyst Activity and Iron Time Yield. The carbon dioxide hydrogenation reaction ($\text{H}_2/\text{CO}_2 = 3$, $P = 10 \text{ bar}$, $T = 350 \text{ }^{\circ}\text{C}$) yielded CO, methane, C_2 – C_4 paraffins, olefins, and C_{5+} hydrocarbons (until C_{12}). There was no evidence of oxygenated compounds or long-chain liquid hydrocarbons. The CO_2 conversions in the range from 25% to 45% were obtained by adjusting the gas-space velocity. This conversion range allowed accurate measurements of the overall CO_2 hydrogenation rates and product selectivities. The catalytic activity is expressed as the iron time yield (FTY) for each catalyst (Figure 1). Note that the promotion with Sb, Bi, and

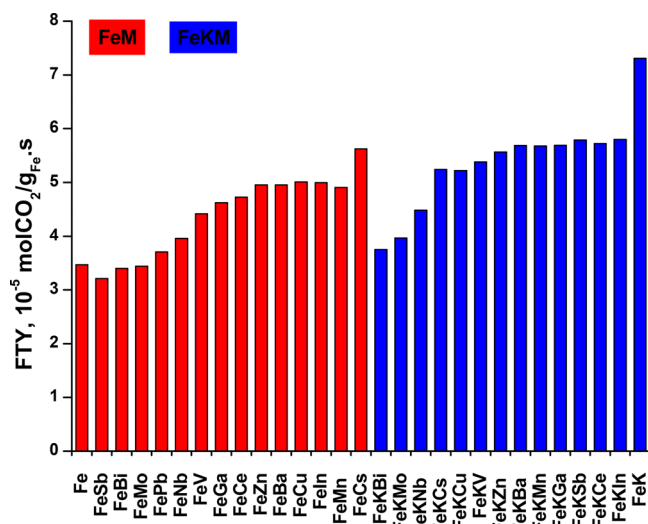


Figure 1. Carbon dioxide conversions and iron time yields (FTY) measured over the promoted zirconia-supported iron catalysts. $T = 350 \text{ }^{\circ}\text{C}$, $\text{H}_2/\text{CO} = 3$, $p = 10 \text{ bar}$, TOS = 50 h.

Mo seems to have a slightly negative effect on the catalyst activity. All other promoted catalysts exhibited higher activities than the reference unpromoted Fe/ZrO_2 . The most pronounced increase in the reaction rate was observed over the potassium and cesium promoted catalysts. The iron time yield almost doubled after the addition of 1.5 wt % of potassium. Interestingly, the combined promotion with potassium and a second element generally led to higher reaction rates, as compared to the promotion without potassium.

3.1.2. Product Selectivity at Different Conversions. The selectivities of CO_2 hydrogenation to carbon monoxide and hydrocarbons measured at different WHSV values are shown in Figures 2–6. At lower CO_2 conversions, the selectivity to

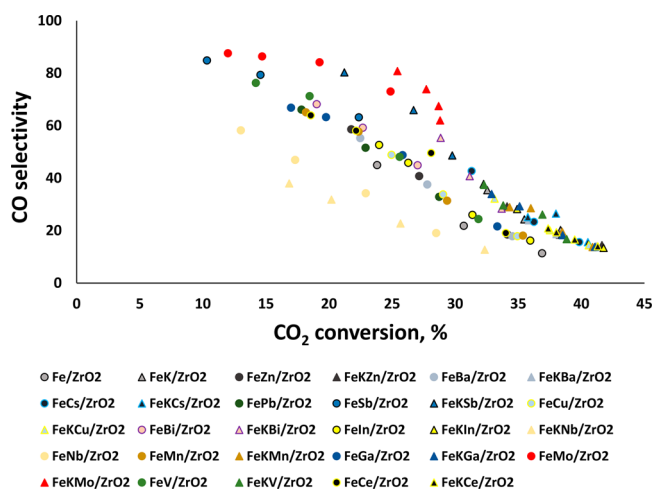


Figure 2. CO selectivity versus carbon dioxide conversion for the Fe/ZrO_2 promoted catalysts. $T = 350 \text{ }^{\circ}\text{C}$, $\text{H}_2/\text{CO} = 3$, WHSV = 4.67–18.19 L/g·h, $P = 10 \text{ bar}$, TOS = 50 h.

CO is very high; the extrapolation of CO selectivity to the zero CO_2 conversion yields almost 100%. The CO selectivity decreases as a function of CO_2 conversion (Figure 2). The CO selectivity drops to 10% at the CO_2 conversions exceeding 40%. Carbon monoxide seems to be produced by RWGS. Extremely high CO selectivity (>90%) at a low CO_2 conversion and extrapolation to 100% at zero CO_2 conversion suggest that CO is the primary product of CO_2 hydrogenation over iron catalysts. Thus, the CO_2 -FT synthesis proceeds via the intermediate formation of carbon monoxide.

Note that the CO selectivity at the same conversion varies for different catalysts. The CO selectivity was particularly high over the antimony and molybdenum promoted catalysts, while a somewhat lower CO selectivity was observed over the niobium promoted samples. Interestingly, the promoted iron catalysts containing potassium show a higher CO selectivity at the same conversion (except for the catalyst promoted with Nb), as compared to the promoted iron catalysts without potassium (Figure 2).

A similar trend was observed for the CH_4 selectivity (Figure 3). The methane selectivity (excluding carbon monoxide) was relatively high at low CO_2 conversion on all catalysts approaching 80% at the conversion below 5%. An increase in the CO_2 conversion results in a drop in the methane selectivity and the production of C_{2+} hydrocarbons. Similar behavior for methane selectivity was previously reported⁶⁷ in FT synthesis with syngas over promoted iron catalysts. A higher methane

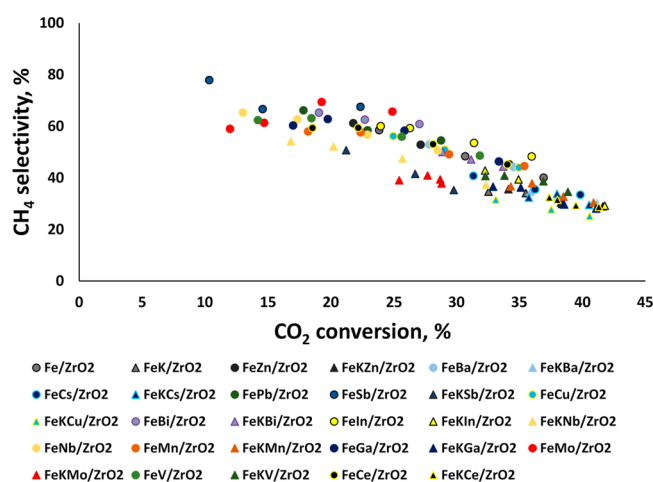


Figure 3. Methane selectivity versus carbon dioxide conversion for Fe/ZrO₂ promoted catalysts. $T = 350\text{ }^{\circ}\text{C}$, $\text{H}_2/\text{CO} = 3$, WHSV = 4.67–18.19 L/g·h, $P = 10\text{ bar}$, TOS = 50 h.

selectivity was observed over the FeMo/ZrO₂, FeBi/ZrO₂, FeIn/ZrO₂, and FeSb/ZrO₂ samples (Figure 3). Addition of potassium with the second promoter results in a decrease in the methane selectivity over all promoted iron catalysts.

The light olefin selectivity data are displayed in Figure 4. The dependence of light olefin selectivity (Figure 4) on the

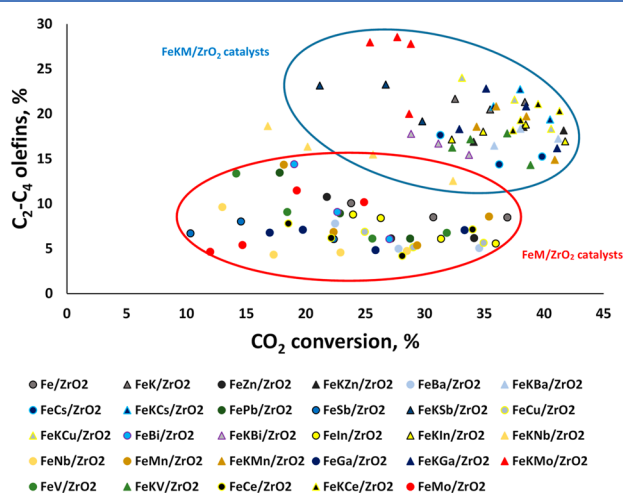


Figure 4. Light olefin selectivity versus carbon dioxide conversion for Fe/ZrO₂ promoted catalysts. $T = 350\text{ }^{\circ}\text{C}$, $\text{H}_2/\text{CO} = 3$, WHSV = 4.67–18.19 L/g·h, $P = 10\text{ bar}$, TOS = 50 h.

CO₂ conversion shows two different behaviors. The first trend is observed for the promoted iron catalysts, which do not contain alkaline metals (potassium or cesium). The light olefin selectivity varies between 5% and 15% and is not, to any noticeable extent, affected by the CO₂ conversion level. The second trend is seen for the promoted iron catalysts containing potassium or cesium. The alkaline containing catalysts show higher light olefin selectivities. The light olefin selectivity shows some decrease, when the CO₂ conversion increases. Figure 4 has allowed identification of the most efficient promoters for iron catalysts. Clearly, the presence of potassium is essential to obtain a higher light olefin selectivity. In addition to potassium, Mo, Cu, Cs, Ce, and Ga seem to be efficient promoters, further increasing the selectivity of CO₂ hydro-

genation to light olefins. The phenomenon is more pronounced for the FeKM/ZrO₂ catalyst.

Let us now consider the variation of light paraffin and C₅₊ hydrocarbon selectivities with the CO₂ conversion over the promoted iron catalysts. The FeM/ZrO₂ catalysts, which do not contain alkaline metals, show a noticeable increase in the C₂–C₄ paraffin selectivity with the CO₂ conversion (Figure 5).

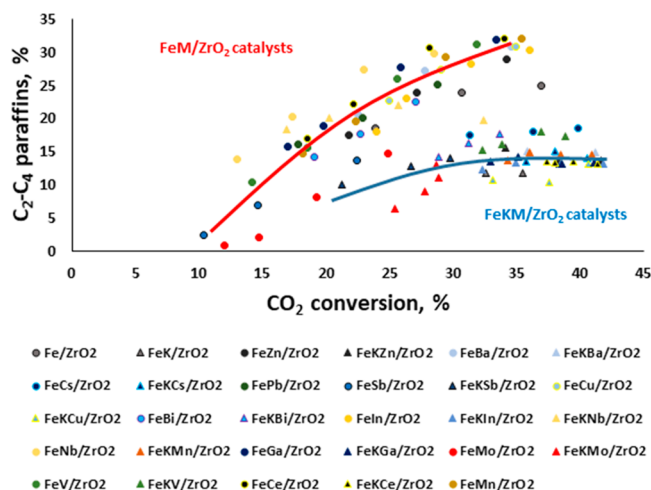


Figure 5. C₂–C₄ paraffins selectivity versus carbon dioxide conversion for Fe/ZrO₂ promoted catalysts. $T = 350\text{ }^{\circ}\text{C}$, $\text{H}_2/\text{CO} = 3$, WHSV = 4.67–18.19 L/g·h, $P = 10\text{ bar}$, TOS = 50 h.

The light paraffin selectivity increases from 0 to 35%, as the CO₂ conversion rises from 10% to 40%. This suggests that, on the one hand, the C₂–C₄ paraffins seem to be secondary products over iron catalysts. They probably originate from the hydrogenation of light olefins or C_nH_m surface species, which can be common precursors of both light olefins or paraffins. On the other hand, the FeKM/ZrO₂ catalysts, that is, with potassium, present a much smaller variation of the C₂–C₄ paraffin selectivity with the CO₂ conversion (Figure 5). This suggests that secondary hydrogenation of light olefins or common surface precursors would be less significant in the presence of alkaline promoters. Instead, over the latter catalysts, higher CO₂ conversion results in the increase in the selectivity to the C₅₊ hydrocarbons (Figure 6). Finally, in contrast to FeKM/ZrO₂, over the FeM/ZrO₂ catalysts, the C₅₊ selectivity, which varies between 5% and 20%, seems to be less dependent on the CO₂ conversion.

The catalyst stability is another important characteristic of CO₂ hydrogenation to light olefins. The stability was further tested in a fixed bed reactor. The catalyst results obtained with the laboratory fixed bed reactor show similar trends as compared to the results measured in the HTE tests. Figure S1 shows the CO₂ conversion as a function of time-on-stream during 48 h of reaction. It is clear that the Fe/ZrO₂ reference catalyst deactivates with the reaction time, and the CO₂ conversion drops from 20% to 8%. All of the studied promoted catalysts showed higher activity than the reference catalyst (up to 7 times higher). In the case of the catalysts promoted only with K, the activity increases up to 4 times as compared to the reference Fe/ZrO₂ catalyst, while a second promoter further enhances the activity as compared to the catalysts promoted solely with an alkaline metal. Note that not only the activity but also the stability was enhanced in the presence of these promoters. The light olefin selectivity did not significantly

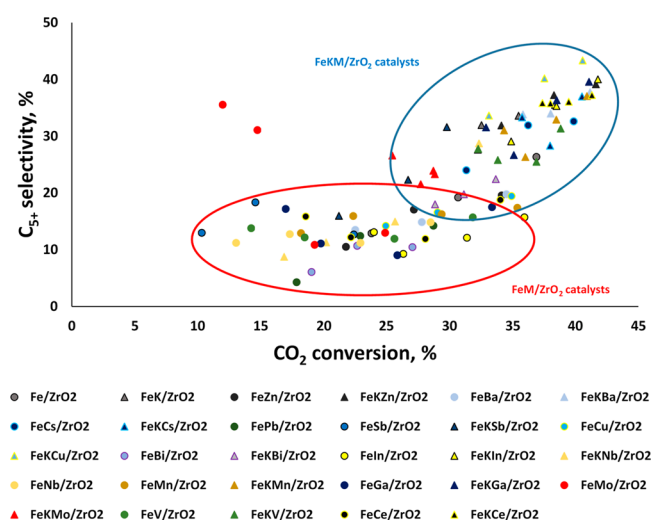


Figure 6. C_{5+} selectivity versus carbon dioxide conversion for Fe/ ZrO_2 promoted catalysts. $T = 350\text{ }^{\circ}\text{C}$, $H_2/CO = 3$, WHSV = 4.67–18.19 L/g·h, $P = 10\text{ bar}$, TOS = 50 h.

change during the reaction with the exception of FeKMo/ ZrO_2 , which shows a steady increase in the light olefin selectivity with the reaction time.

To provide further insights into the enhancement of the catalytic performance on the promotion, the Fe/ ZrO_2 (reference), FeK/ ZrO_2 , FeKMo/ ZrO_2 , FeKCu/ ZrO_2 , FeKCs/ ZrO_2 , FeKCe/ ZrO_2 , and FeKGa/ ZrO_2 catalysts have been investigated by a combination of characterization techniques.

3.2. Catalyst Characterization. The XRF elemental analysis data for selected promoted iron catalysts are displayed in Table 1. All of the catalysts have similar iron contents close to nominal value (around 10 wt %). At the same time, the potassium content was slightly higher than expected (around 1.5 wt %), while the amount of Cs, Ce, Cu, and Ga was as expected, 50:1 in molar ratio relative to iron. Only the Mo promoted catalyst shows a higher promoter content. The calcined catalysts display characteristic XRD peaks (Figure 7a) attributed to the zirconia support.^{71,72} The XRD peaks located at 28.2° and 31.5° are assigned to monoclinic zirconia (JCPDS 37-1484), while the peak at 50.3° reveals the presence of tetragonal zirconia (JCPDS 17-0923). Even though some broad hematite (Fe_2O_3 , JCPDS13-0534) peaks were detected, the intensity of them was rather low. Significant broadening of these peaks indicates the small size of iron oxide nanoparticles

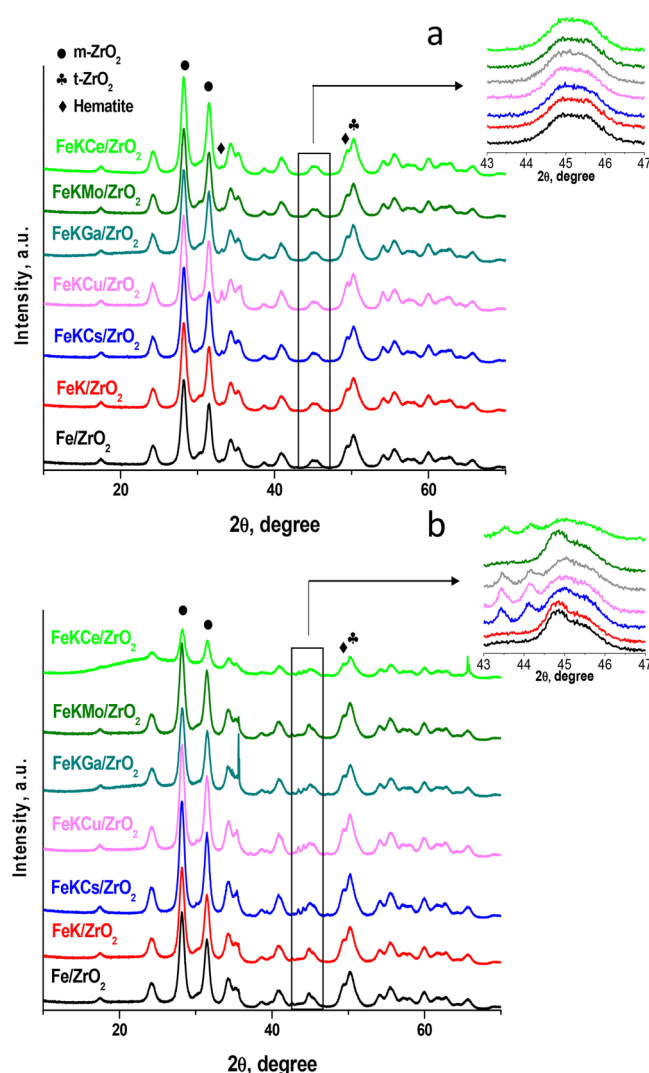


Figure 7. XRD patterns of the catalysts after calcination (a) and after reaction (b).

(below 5 nm). No diffraction peaks assignable to the crystalline phases of promoters were observed. This is attributed to their low content in the catalysts.

We also performed XRD measurements (Figure 7b) for reference and promoted catalysts after conducting the CO_2 hydrogenation reaction. The spent FeKCs/ ZrO_2 , FeKCu/ ZrO_2 , FeKGa/ ZrO_2 , and FeKGa/ ZrO_2 catalysts exhibit new

Table 1. Properties of Selected Supported Fe Catalysts

sample	Fe content ^a (wt %)	K content ^a (wt %)	promoter content ^a (wt %)	total H_2 consump. ^b (mmol/g)	S_{BET} ^c (m^2/g)	V_{tot} ^d (cm^3/g)	CO_2 ads. from TPD ($\mu mol/g$)	TOF ^e (s^{-1})
ZrO_2					95.6	0.286	197.5	
Fe/ ZrO_2	10.09			1.81	70.0	0.212	46.9	0.13
FeK/ ZrO_2	10.35	1.51		2.01	57.6	0.171	388.2	0.26
FeKCs/ ZrO_2	9.66	1.11	1.05	2.45	58.4	0.173	474.4	
FeKCu/ ZrO_2	10.22	1.56	0.77	2.16	66.8	0.200	342.0	
FeKGa/ ZrO_2	10.38	1.46	0.33	2.62	47.6	0.174	312.9	0.50
FeKMo/ ZrO_2	10.36	1.53	2.87	2.86	64.3	0.185	102.3	0.15
FeKCe/ ZrO_2	11.01	1.47	0.97	2.70	65.4	0.176	246.0	

^aFe and promoter content from XRF. ^bThe total H_2 consumption from TPR analysis. ^cBET surface area. ^dSingle point desorption total pore volume of pores, $P/P_0 = 0.975$. ^eTOF was calculated⁷⁰ from the average size of the iron carbide nanoparticles in the activated catalysts using the density of Hägg iron carbide Fe_5C_2 ($\rho = 7.57\text{ g/cm}^3$) and assuming 14 Fe atoms/nm².

diffraction peaks at 2θ angles of 43.4° and 44.1° that can be attributed to the iron carbide phases such as Hägg iron carbide (Fe_5C_2 , JCPDS20-0509) formed during the reaction. Because of the similarity of XRD patterns attributed to different iron carbides, identification of individual iron carbide phases by means of XRD analysis is challenging.

Figure 8 shows the CO_2 TPD curves for the promoted iron catalysts, while the amount of CO_2 adsorbed over the catalysts

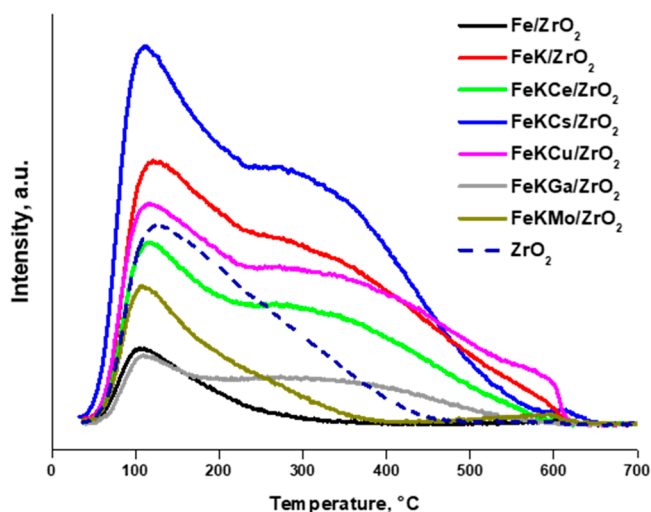


Figure 8. CO_2 TPD profiles adsorbed over ZrO_2 and iron catalysts.

is shown in Table 1 and Table S1. The profiles exhibit three peaks: the first one located at $80\text{--}100^\circ\text{C}$, corresponding to weak basic sites, the second one at $150\text{--}200^\circ\text{C}$ assigned to medium basic sites, and the third one at 350°C attributed to strong basic sites. The deconvolution of the CO_2 -TPD profiles is illustrated in Figure S2. ZrO_2 is a basic oxide, and the TPD profile of pure zirconia is similar to that previously reported in the literature.^{73,74} The deconvolution (Figure S2) displays two broad CO_2 TPD peaks at 100 and 220°C . This suggests the presence of a wide range of relatively weak and medium basic sites. Addition of iron to ZrO_2 reduces the CO_2 -TPD peak intensity. It seems that some medium basic sites of zirconia are neutralized by added iron oxides. The promotion with potassium and cesium leads to an increase in the number of adsorbed CO_2 and results in two distinct peaks, the first at 120°C corresponding to the weak basicity and the second at $300\text{--}420^\circ\text{C}$ corresponding to stronger basicity. The intensity of these peaks correlates with the amount of alkaline metals in the catalysts. Addition of the second promoter (except for Cs) results in a decreasing concentration of basic sites, indicating some interaction of the promoter with potassium and zirconia. Such a lower concentration of basic sites has been observed in the iron catalyst simultaneously promoted with potassium and molybdenum (Figure 8).

The TPR profiles of the reference Fe/ZrO_2 , FeK/ZrO_2 , $\text{FeKCs}/\text{ZrO}_2$, $\text{FeKCe}/\text{ZrO}_2$, and $\text{FeKGa}/\text{ZrO}_2$ catalysts are displayed in Figure 9. The amount of hydrogen consumed for catalyst reduction is given in Table 1. The first reduction peak at $\sim 380^\circ\text{C}$ can be attributed to the hematite reduction to magnetite, $\text{Fe}_2\text{O}_3 \rightarrow \text{Fe}_3\text{O}_4$,⁷⁵ and the second broader peak is related to the successive reduction of iron oxides, $\text{Fe}_3\text{O}_4 \rightarrow \text{FeO} \rightarrow \text{Fe}$.^{76–78} This second peak is centered at $\sim 500^\circ\text{C}$ for the reference Fe/ZrO_2 and FeK/ZrO_2 catalysts.

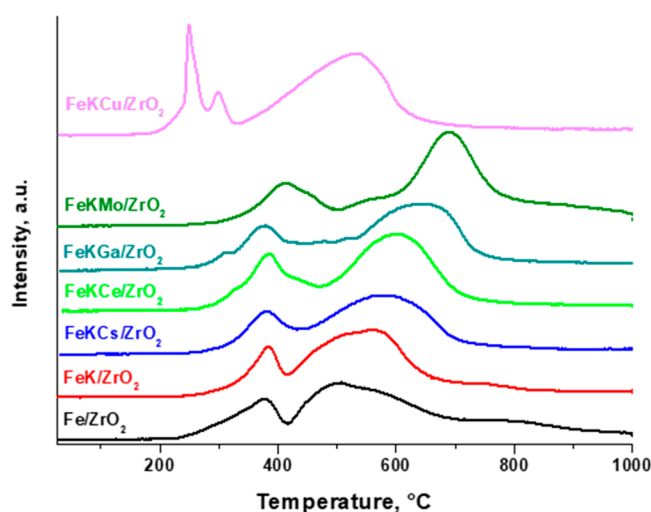


Figure 9. H_2 -TPR profiles of the reference catalysts and catalysts promoted with K, Cs, Ce, Ga, Mo, and Cu.

For the $\text{FeKCs}/\text{ZrO}_2$, $\text{FeKCe}/\text{ZrO}_2$, $\text{FeKMo}/\text{ZrO}_2$ and $\text{FeKGa}/\text{ZrO}_2$ catalysts, this peak shifts toward higher temperatures. Addition of Cs, Ga, Mo and Ce seems to give place to a strong interaction of iron oxide with the promoters⁷⁹ and hinders reduction of the magnetite phase. Note that these promoters do not affect the first reduction step (Fe_2O_3 to Fe_3O_4). However, the H_2 -TPR profile of $\text{FeKMo}/\text{ZrO}_2$ shows a shift to higher temperatures for both peaks.

So, the molybdenum presence clearly affects the different iron oxide reduction steps. Finally, the H_2 -TPR profile of $\text{FeKCu}/\text{ZrO}_2$ displays two reduction peaks at ~ 250 and 298°C , which shift to lower temperatures as compared to the reference Fe/ZrO_2 sample, in agreement with the literature.⁷⁵ The intensity of the peak at 250°C can also contribute from the reduction of copper.⁸⁰ Indeed, the presence of copper in the catalyst may facilitate iron oxide reduction. Remarkably, the addition of promoters results in a higher amount of consumed hydrogen (Table 1). It seems that the promotion slows the interaction of iron with zirconia and increases the amount of reducible iron. Note that the amounts of incorporated promoters as compared to iron are rather small to significantly contribute to the intensity of the TPR peaks.

The information about the dispersion of iron and localization of promoters was extracted from the STEM-HAADF and STEM-EDS analyses of the activated iron catalysts. The high-resolution STEM images of the reference Fe/ZrO_2 catalyst, FeK/ZrO_2 , $\text{FeKGa}/\text{ZrO}_2$, and $\text{FeKMo}/\text{ZrO}_2$ are shown in Figure S3. The catalysts show agglomerated nanoparticles with mainly oval shape and narrow size distribution from 6 to 27 nm. The average catalyst particle size was around 14 nm for all studied catalysts. No clear signature of Ga and K was observed in the images, because of their small amounts and their Z number relatively close to that of Fe and Zr. At the same time, because of a noticeable Z-contrast in the STEM-HAADF mode, atoms and atomic clusters of Mo are visible as light spots and agglomerates in $\text{FeKMo}/\text{ZrO}_2$ (Figure S4).

The STEM-HAADF and STEM-EDS images have provided further more precise information about iron particle sizes and promoter localization in the supported catalysts (Figure 10). The histograms of iron nanoparticle sizes were estimated from the STEM-EDS Fe elemental maps. In the reference Fe/ZrO_2

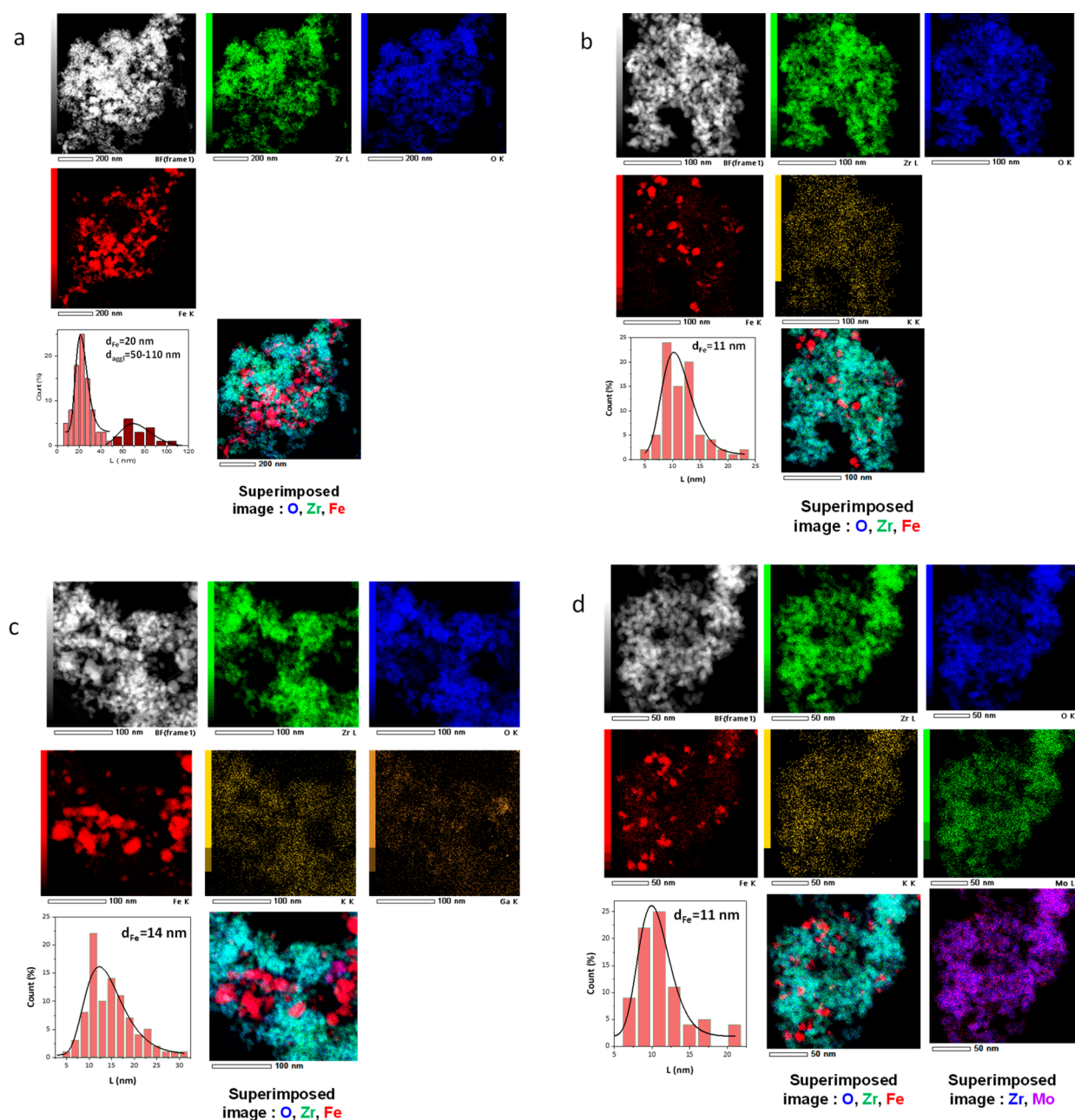


Figure 10. STEM-HAADF, SEM-EDX mapping, and histograms of iron nanoparticle sizes for the activated Fe/ZrO₂ (a), FeK/ZrO₂ (b), FeKGa/ZrO₂ (c), and FeKMo/ZrO₂ (d) catalysts.

sample, iron nanoparticles of 20 nm mean diameter were homogeneously dispersed in the ZrO₂ matrix. Local agglomeration of iron nanoparticles was also observed. This is most probably due to the fact that TEM acquires a projection of the volume, and, therefore, the superposition of nanoparticles in the projection within the analyzed volume leads to a certain agglomeration of nanoparticles. Interestingly, a relatively low concentration of oxygen was found in the iron-rich areas as compared to the iron-poor ones (Figure S5). This could be indicative of a lower fraction of iron oxides and a higher extent of iron carbidization in the activated catalysts. Because the specimens were deposited onto carbon supports, it is difficult to estimate the carbon content in the samples. This is due to the superposition of the carbon signal from the membrane and the occurrence of carbon contamination during the long duration scanning. The promoted FeK/ZrO₂, FeKGa/ZrO₂,

and FeKMo/ZrO₂ catalysts exhibited much smaller iron nanoparticles of 11–14 nm homogeneously dispersed within the ZrO₂ matrix, without any Fe nanoparticle agglomeration (Figure 10). The promoters (K, Ga, and Mo) appear to be homogeneously distributed in very small amounts. EDS also confirmed nearly atomic Mo distribution over zirconia (Figure S4).

To gain a deeper understanding of the catalytic performance, the reference and promoted iron catalysts were characterized using *in situ* Mössbauer spectrometry under the flow of CO and reaction gas mixture (CO₂ + H₂). After the CO activation at 350 °C (Figure 11), iron Hägg carbide and wüstite (FeO) were observed in all of the samples. The promotion of Fe/ZrO₂ catalyst with K and Mo results in a higher fraction of iron carbide (Table 2). A noticeable concentration of metastable

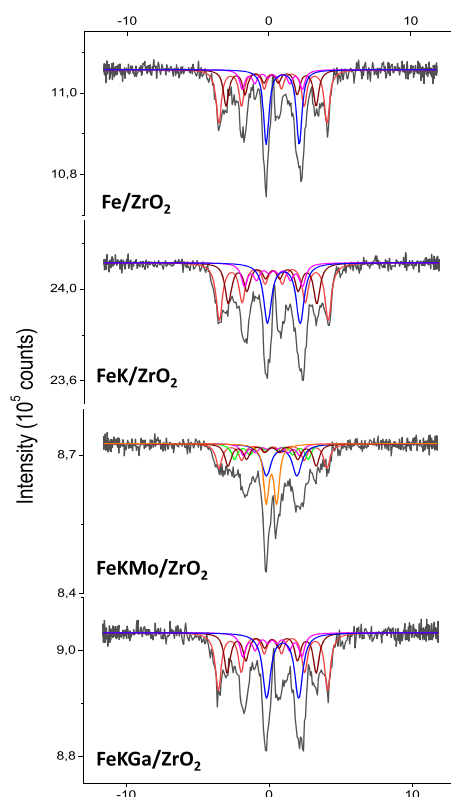


Figure 11. Mössbauer spectra after activation measured at $-153\text{ }^{\circ}\text{C}$.

(ϵ' - $\text{Fe}_{2.2}\text{C}$) carbide (ref 63) was observed in the FeKMo/ZrO₂ catalyst after the activation.

Figure 12 shows the in situ Mössbauer spectra after catalyst exposure to the reaction conditions ($\text{H}_2/\text{CO}_2 = 3$, $350\text{ }^{\circ}\text{C}$ and 10 bar). Two types of Mössbauer spectra modification were observed. On the one hand, there is a slight improvement in the crystallinity of the Hägg iron carbide species. In the Mössbauer spectroscopy, the crystallinity was reflected by the line width of the measured signal. The reference Fe/ZrO₂ catalyst after 24 h of reaction exhibits better defined Hägg structures. The line width of the Mössbauer signals decreased from 0.45 to 0.42 mm/s (Table 2).

The same tendency was observed for all promoted catalysts. On the other hand, the fraction of iron carbide seems to further increase after the CO₂ hydrogenation. This is shown by the lower amount of unreduced wüstite species in the spent catalysts as compared to that in the counterparts activated in CO. In contrast to other catalysts, FeKGa/ZrO₂ after reaction did not show any increase in the iron carbide content, indicating a smaller effect of Ga addition on iron carbidization. Only the slightly smaller line width values indicate the presence of better defined Hägg carbide species in FeKGa/ZrO₂ as compared to FeK/ZrO₂. Note that the FeKMo/ZrO₂ catalyst showed the higher fraction of iron carbide among all studied promoted iron catalysts after the CO₂ hydrogenation.

Carbon deposition can result in a loss of catalytic activity in the CO₂ hydrogenation. Figure S6 shows the thermogravimetric analysis (TGA) data for the spent ZrO₂-supported catalysts. The first small loss around $150\text{ }^{\circ}\text{C}$ is normally generated by the water desorption and possible dehydration of iron oxyhydroxide (FeOOH).⁶¹ Above $300\text{ }^{\circ}\text{C}$, significant weight losses produced by the combustion of carbon deposits and carbides can be observed. Interestingly, the reference

catalyst presents a smaller weight loss relative to the promoted counterparts. So, the enhancement of stability observed during the CO₂ hydrogenation reaction over the promoted catalysts (Figure S1) seems not to be related to the catalyst's ability to avoid carbon deposition and can possibly be assigned to other phenomena. One possible reason for the better stability of the catalysts could be related to less noticeable sintering of the iron carbide nanoparticles after the addition of the promoters.

4. DISCUSSION

CO₂-FT synthesis occurs at $300\text{--}350\text{ }^{\circ}\text{C}$ and focuses on the production of light olefins. As compared to the “methanol-mediated” processes occurring over metal–oxide/zeolite catalysts, CO₂-FT synthesis exhibits higher yields of olefins and lower selectivity to CO.^{32,33} The selection of efficient promoters for iron catalysts seems to be the key for the selectivity control of this reaction. Alkaline metals,^{35,38–47} copper,^{53,54} manganese,^{46,47,55} zinc,^{32,45,56,57} and cobalt^{48–52} have been the most investigated promoters for iron CO₂-FT catalysts. At the same time, very limited attention has been paid to the promotion of iron CO₂-FT catalysts with other elements. In this work, HTE combined with catalyst characterization have allowed the identification of new efficient promoters and also provided important information about the influence of these promoters on reaction elementary steps.

CO₂-FT synthesis is a complex multistage reaction.^{23,24,43,81} Different reaction stages can be affected to a different extent by the promotion. The experimental results shown in Figures 2–6 illustrate the effects of added promoters on the product selectivity. Figure 2 shows the CO selectivity close to 100% at the CO₂ conversion approaching zero. CO seems indeed to be the primary product of CO₂ hydrogenation over iron catalysts. Importantly, the experimental results obtained for numerous promoted iron catalysts exhibit a similar trend. RWGS is a fast reaction and is readily catalyzed by iron oxides (e.g., Fe₃O₄).^{32,43} The presence of noticeable concentrations of iron oxide species in the working catalysts has been identified by Mössbauer spectrometry. Interestingly, almost all promoted catalysts showed a much higher CO selectivity at the same CO₂ conversion as compared to the reference Fe/ZrO₂ catalyst. The added promoters could therefore contribute to RWGS. This also coincides with a higher overall activity (FTY) of the promoted catalysts compared to the reference (Figure 1).

The methane selectivity versus conversion curve (Figure 3) also agrees with the suggested reaction sequence (Figure 13). Higher methane selectivity is observed at lower CO₂ conversion, and then the methane selectivity drops at higher conversion. At low conversion, hydrogenation of C₁ monomer seems to prevail over its oligomerization. At a higher CO₂ conversion and a higher surface concentration of C₁ monomers, their oligomerization becomes more favorable and leads to the adsorbed C₂–C₄ species. This trend has been seen for all catalysts, with somewhat lower methane selectivity at the same conversions observed for FeMo/ZrO₂, FeKMo/ZrO₂, and FeKSb/ZrO₂.

Very different correlations between light olefin selectivity and conversion have been observed for the catalysts with and without alkaline metals (Figure 4). The light olefin selectivity over FeM/ZrO₂ (without alkaline metals) was much lower as compared to the FeKM/ZrO₂ catalysts promoted with potassium, and it does not noticeably vary as a function of CO₂ conversion. The higher selectivity to light olefins over the

Table 2. Mössbauer Fitted Parameters of the ZrO₂-Based Catalysts, Obtained at −153 °C^a

sample/treatment	IS (mm s ^{−1})	QS (mm s ^{−1})	hyperfine field (T)	Γ (mm s ^{−1})	phase	spectral contribution (%)
Fe/ZrO ₂	0.28		23.7	0.45	χ-Fe ₅ C ₂ (I)	36
CO, 350 °C	0.16		19.7	0.45	χ-Fe ₅ C ₂ (II)	25
	0.24		13.2	0.45	χ-Fe ₅ C ₂ (III)	13
	0.98	2.32		0.45	Fe _{1−x} O (SPM ^b)	26
Fe/ZrO ₂	0.28		23.7	0.42	χ-Fe ₅ C ₂ (I)	37
H ₂ /CO ₂ = 3, 350 °C, 10 bar	0.15		19.8	0.42	χ-Fe ₅ C ₂ (II)	27
	0.17		13.6	0.42	χ-Fe ₅ C ₂ (III)	12
	1.00	2.35		0.47	Fe _{1−x} O (SPM)	24
FeK/ZrO ₂	0.26		23.7	0.54	χ-Fe ₅ C ₂ (I)	37
CO, 350 °C	0.18		19.3	0.54	χ-Fe ₅ C ₂ (II)	26
	0.24		12.6	0.54	χ-Fe ₅ C ₂ (III)	14
	0.96	2.28		0.65	Fe _{1−x} O (SPM)	23
FeK/ZrO ₂	0.27		23.8	0.47	χ-Fe ₅ C ₂ (I)	36
H ₂ /CO ₂ = 3, 350 °C, 10 bar	0.17		19.9	0.47	χ-Fe ₅ C ₂ (II)	29
	0.24		12.8	0.47	χ-Fe ₅ C ₂ (III)	16
	1.00	2.31		0.58	Fe _{1−x} O (SPM)	19
FeKMo/ZrO ₂	0.28		23.5	0.53	χ-Fe ₅ C ₂ (I)	20
CO, 350 °C	0.23		19.2	0.53	χ-Fe ₅ C ₂ (II)	18
	0.20		11.2	0.53	χ-Fe ₅ C ₂ (III)	10
	0.17		16.1	0.53	ε'-Fe _{2.2} C	13
	0.17	0.74		0.45	Fe _x C (SPM)	20
	0.90	2.15		0.77	Fe _{1−x} O (SPM)	19
FeKMo/ZrO ₂	0.27		23.7	0.49	χ-Fe ₅ C ₂ (I)	25
H ₂ /CO ₂ = 3, 350 °C, 10 bar	0.21		19.6	0.49	χ-Fe ₅ C ₂ (II)	24
	0.20		10.9	0.49	χ-Fe ₅ C ₂ (III)	11
	0.22		16.6	0.49	ε'-Fe _{2.2} C	14
	0.14	0.70		0.28	Fe _x C (SPM)	10
	1.02	2.35		0.61	Fe _{1−x} O (SPM)	16
FeKGa/ZrO ₂	0.26		23.8	0.50	χ-Fe ₅ C ₂ (I)	35
CO, 350 °C	0.19		19.3	0.50	χ-Fe ₅ C ₂ (II)	24
	0.22		12.3	0.50	χ-Fe ₅ C ₂ (III)	14
	0.95	2.24		0.67	Fe _{1−x} O (SPM)	27
FeKGa/ZrO ₂	0.28		23.9	0.43	χ-Fe ₅ C ₂ (I)	36
H ₂ /CO ₂ = 3, 350 °C, 10 bar	0.19		20.0	0.43	χ-Fe ₅ C ₂ (II)	29
	0.26		12.7	0.43	χ-Fe ₅ C ₂ (III)	17
	0.99	2.38		0.57	Fe _{1−x} O (SPM)	18

^aExperimental uncertainties: isomer shift, IS ± 0.02 mm s^{−1}; quadrupole splitting, QS ± 0.02 mm s^{−1}; line width, Γ ± 0.03 mm s^{−1}; hyperfine field, ±0.1 T; spectral contribution, ±3%. ^bVery small, superparamagnetic (SPM).

FeKM/ZrO₂ catalysts decreases as a function of CO₂ conversion. For the catalysts without alkaline promoters, increased CO₂ conversion results in higher selectivity to C₂–C₄ hydrocarbons, while for the catalysts containing alkaline metals, higher selectivity to the C₅₊ paraffins was measured at higher CO₂ conversions (Figure 5). Higher conversion leads therefore to a higher selectivity to the C₅₊ hydrocarbons, which can be attributed to enhanced surface oligomerization of C₁ monomeric species and readsorption of light olefins,^{82,83} which may reinitialize oligomerization on iron catalysis, both phenomena favoring the production of longer-chain hydrocarbons.

The possible reaction paths of CO₂-FT synthesis over iron catalysts have been summarized in Figure 13. The first step in CO₂-FT synthesis over iron catalysts is CO₂ hydrogenation to CO (RWGS) followed by the formation of C₁ adsorbed monomers. The adsorbed C₁ monomers then either can be hydrogenated to yield methane or undergo oligomerization to different C_n adsorbed species. Desorption of C₂–C₄ adsorbed species should produce light olefins (ethylene, propylene, or butylene), while their hydrogenation leads to light paraffins,

the latter also possibly are produced via olefin readsorption (and subsequent hydrogenation).^{84–86} Further reactions of adsorbed C₂–C₄ species with C₁ monomer produce longer-chain hydrocarbons.

The rates of hydrogenation of adsorbed C₂–C₄ species and rates of oligomerization seem to be different over the catalysts with (Figure 13a) and without potassium (Figure 13b). These phenomena also explain the role of alkaline promoters. The promotion with alkaline metals results in a decrease in the catalyst hydrogenation ability and, at the same time, increases the rate of oligomerization of C₁ surface monomers. Thus, over the catalysts containing alkaline metals, the oligomerization limits the light olefin selectivity, while the contributions of the hydrogenation of the adsorbed C₂–C₄ species or the secondary hydrogenation of light olefins are not significant. This suggests that, to boost the light olefin selectivity over the catalysts promoted with alkaline metals, the surface oligomerization should be hindered after the formation of the C₄ surface fragments. Similar effects were previously observed in the CO hydrogenation over iron catalysts.⁶⁷ The second promoter should, therefore, slow chain growth in particular for

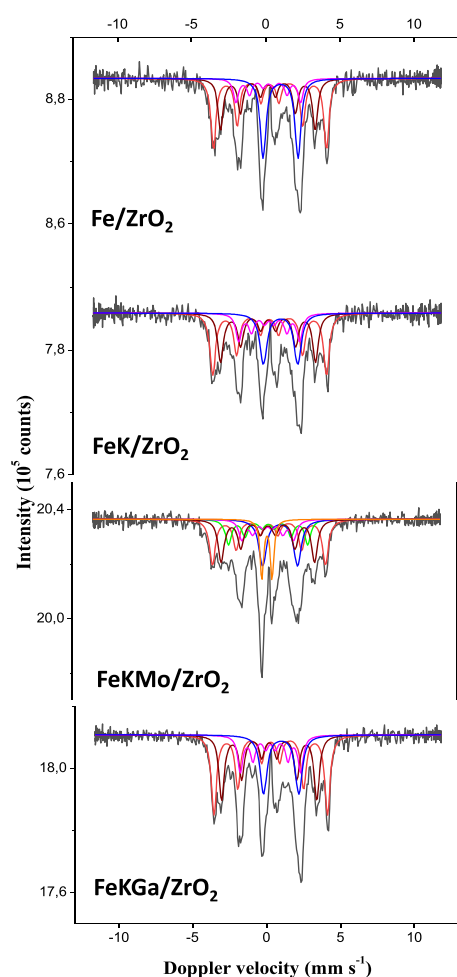


Figure 12. Mössbauer spectra after reaction measured at $-153\text{ }^{\circ}\text{C}$.

C_{5+} hydrocarbon fragments, without any enhancement of hydrogenation.

The key issue in the catalyst design for CO_2 -FT synthesis is therefore light olefin selectivity. Figure 4 shows the light olefin selectivity versus conversion, and it enables the identification of the most efficient second promoters such as Mo, Cs, Ga, Ce,

and Cu. Note that, to reach a higher selectivity to light olefins, these promoters should be used in combination with potassium.

The catalyst promoters are usually divided into two types: (i) structural promoters, which might generate an enhanced iron dispersion and carbidization and give better mechanical resistance, and (ii) electronic promoters, which could enhance the intrinsic activity of active sites (TOF). Several phenomena can be responsible for the observed increase in the light olefin selectivity over the catalysts promoted simultaneously with potassium and other elements. First, the STEM-HAADF and STEM-EDS images of the promoted catalysts (Figure 10) showed a noticeable increase in the iron dispersion in the activated catalysts compared to the reference Fe/ZrO_2 counterpart. Consequently, a higher iron dispersion can contribute to the increase in FT reaction rate and light olefin selectivity. Second, the addition of promoters can modify the extent of iron carbidization and reduction. The in situ Mössbauer data (Table 2) show that the presence of the promoters such as Mo, K, and Ga results in a higher fraction of iron carbide. For the $\text{FeKMo}/\text{ZrO}_2$ catalyst promoted with potassium and molybdenum, the increase in iron carbidization during the reaction coincides with the continuous increase in light olefin selectivity. The TPR results (Figure 9) show easier iron reduction in the copper-promoted catalysts. Third, the promotion enhances the RWGS reaction, which is an important step in CO_2 -FT synthesis and often affects the overall activity. Indeed, most of the promoted catalysts showed higher CO selectivity at a given CO_2 conversion as compared to reference Fe/ZrO_2 . Fourth, the promotion affects the catalyst basicity and, hence, the adsorption of CO_2 , which is an acid molecule. The promotion with potassium principally results in the buildup of strong basic sites (Figure 8, Figure S2, and Table S1). Note that extremely strong or weak basicity does not seem to be optimal for obtaining high concentrations of reactive CO_2 adsorbed molecules. The addition of the second promoter mediates the basicity of FeK/ZrO_2 catalysts (Table S1) and thus favors the CO_2 activation. Fifth, TOF calculated from the iron carbide particle size (Table 1) measured by TEM images shows 2–4 times higher values in the presence of K and K–Ga-promoters, while there is a slight

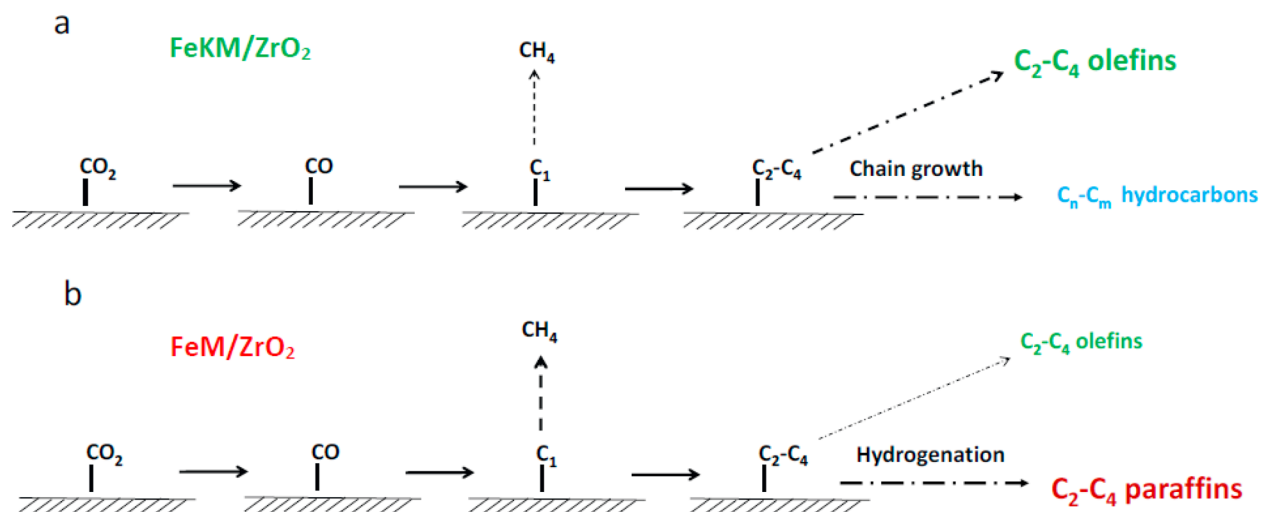


Figure 13. Reaction paths in CO_2 hydrogenation over promoted iron catalysts with (a) and without (b) potassium.

effect of promotion on TOF when Mo is added simultaneously with K.

Light olefin production from CO₂ hydrogenation has important common points with the FT process.⁸⁷ Both are complex polymerization reactions, generally performed in the same conditions of pressure and temperature. Both of them use iron as the main active phase when the C₂–C₄ olefins are desired. Even though CO and CO₂ hydrogenation are similar processes, different mechanisms seem to be ruling these reactions. In our previous works,^{67,88} we demonstrated that light olefin production from CO proceeded more easily, when soldering metals were used as promoters (Bi, Pb, Sn, and Sb) due to a strong Fe–promoter interaction with the formation of core–shell structures and better active phase dispersion. The reaction proceeds via CO chemisorption. The promoter primarily affects the dissociation of the CO molecule, chain growth probability, and secondary hydrogenation. However, for CO₂ hydrogenation, we are faced with a more complex situation. The CO₂ hydrogenation is a combination of RWGS and FT synthesis. This increases the number of reaction elementary steps. Our results show that different promoters contribute to diverse features of the CO₂ hydrogenation catalyst. K brings higher basicity favoring the CO₂ adsorption. Cu addition gives place to better iron reducibility. Mo promotion generates a higher carbonization degree, while, in general, the studied promoted catalysts showed better iron dispersion than did the reference. Each of these promoters contributes to a different extent in the catalyst properties, and from the results presented in this article more than one promoter seems to be needed to enhance the catalytic performance in CO₂ hydrogenation to light olefins.

5. CONCLUSION

HTE tests allowed the identification of new suitable promoters and structure–performance correlations over zirconia-supported iron catalysts for CO₂ hydrogenation to light olefins. The presence of alkaline promoters seems to be indispensable for the selectivity enhancement toward light olefins over iron catalysts. Complementary to potassium, the promotion of ZrO₂-supported catalysts with Cs, Mo, Cu, Ga, and Ce resulted in a further increase in the light olefin selectivity. Better iron dispersion, higher extent of iron carbidization, and optimized basicity coincide with the enhanced light olefin selectivity in the promoted catalysts. The catalyst basicity required for CO₂ adsorption is enhanced by the promotion with alkaline metals and mediated by the second promoter.

CO₂-FT synthesis proceeds via the intermediate production of carbon monoxide. The dependence of light olefin selectivity on the CO₂ conversion exhibits two different trends, depending on potassium promotion. Without potassium as the promoter, the relatively low selectivity to light olefins is practically independent of the CO₂ conversion. The second trend is identified for the iron catalysts containing simultaneously alkaline and second promoter. Over those catalysts, much higher selectivity to light olefins shows a noticeable decrease as a function of CO₂ conversion. Over the catalysts without alkaline metals, a higher CO₂ conversion favors the production of light paraffins, while the presence of potassium leads to higher selectivity toward longer chain hydrocarbons, in particular at a higher conversion level. To obtain high selectivity to light olefins, the second promoter, complementary to an alkaline metal, should hinder chain growth rates

without any increase in the hydrogenation rate of the surface intermediate species.

■ ASSOCIATED CONTENT

Supporting Information

The Supporting Information is available free of charge at <https://pubs.acs.org/doi/10.1021/acscatal.1c05648>.

Conversion and selectivity calculations; CO₂-TPD data; catalyst stability data; STEM-HAADF images; histograms of catalyst particle sizes; results of EDS analysis; and TGA data (PDF)

■ AUTHOR INFORMATION

Corresponding Author

Andrei Y. Khodakov – University of Lille, CNRS, Centrale Lille, University of Artois, UMR 8181 – UCCS – Unité de Catalyse et Chimie du Solide, Lille F-59000, France;
orcid.org/0000-0003-4599-3969;
Email: andrei.khodakov@univ-lille.fr

Authors

Alan J. Barrios – University of Lille, CNRS, Centrale Lille, University of Artois, UMR 8181 – UCCS – Unité de Catalyse et Chimie du Solide, Lille F-59000, France; Laboratory for Chemical Technology (LCT), Department of Materials, Textiles and Chemical Engineering, Ghent University, Ghent B-9052, Belgium
Deizi V. Peron – University of Lille, CNRS, Centrale Lille, University of Artois, UMR 8181 – UCCS – Unité de Catalyse et Chimie du Solide, Lille F-59000, France
Anoop Chakkingal – University of Lille, CNRS, Centrale Lille, University of Artois, UMR 8181 – UCCS – Unité de Catalyse et Chimie du Solide, Lille F-59000, France; Laboratory for Chemical Technology (LCT), Department of Materials, Textiles and Chemical Engineering, Ghent University, Ghent B-9052, Belgium
Achim Iulian Dugulan – Fundamental Aspects of Materials and Energy Group, Delft University of Technology, Delft 2629 JB, Netherlands
Simona Moldovan – Groupe de Physique des Matériaux, CNRS, Université Normandie & INSA Rouen Avenue de l'Université - BP12, St Etienne du Rouvray 76801, France
Kalthoum Nakouri – Groupe de Physique des Matériaux, CNRS, Université Normandie & INSA Rouen Avenue de l'Université - BP12, St Etienne du Rouvray 76801, France
Joëlle Thuriot-Roukos – University of Lille, CNRS, Centrale Lille, University of Artois, UMR 8181 – UCCS – Unité de Catalyse et Chimie du Solide, Lille F-59000, France;
orcid.org/0000-0003-0490-718X
Robert Wojcieszak – University of Lille, CNRS, Centrale Lille, University of Artois, UMR 8181 – UCCS – Unité de Catalyse et Chimie du Solide, Lille F-59000, France;
orcid.org/0000-0002-8956-5846
Joris W. Thybaut – Laboratory for Chemical Technology (LCT), Department of Materials, Textiles and Chemical Engineering, Ghent University, Ghent B-9052, Belgium;
orcid.org/0000-0002-4187-7904
Mirella Virginie – University of Lille, CNRS, Centrale Lille, University of Artois, UMR 8181 – UCCS – Unité de Catalyse et Chimie du Solide, Lille F-59000, France

Complete contact information is available at:
<https://pubs.acs.org/doi/10.1021/acscatal.1c05648>

Notes

The authors declare no competing financial interest.

■ ACKNOWLEDGMENTS

We acknowledge financial support from the European Union (Interreg V project PSYCHE). The REALCAT platform is benefiting from a Governmental subvention administrated by the French National Research Agency (ANR) within the frame of the "Future Investments" program (PIA), with contractual reference "ANR-11-EQPX-0037". GENESIS is supported by the Region Haute-Normandie, the Metropole Rouen Normandie, the CNRS via LABEX EMC, and the French National Research Agency as a part of the program "Future Investments" with the reference ANR-11-EQPX-0020.

■ REFERENCES

- (1) D'Alessandro, D. M.; Smit, B.; Long, J. R. Carbon Dioxide Capture: Prospects for New Materials. *Angew. Chemie-Int. Ed.* **2010**, *49* (35), 6058–6082.
- (2) Aresta, M.; Dibenedetto, A.; Angelini, A. Catalysis for the Valorization of Exhaust Carbon: From CO₂ to Chemicals, Materials, and Fuels. Technological Use of CO₂. *Chem. Rev.* **2014**, *114* (3), 1709–1742.
- (3) Goeppert, A.; Czaun, M.; Jones, J. P.; Surya Prakash, G. K.; Olah, G. A. Recycling of Carbon Dioxide to Methanol and Derived Products-Closing the Loop. *Chem. Soc. Rev.* **2014**, *43* (23), 7995–8048.
- (4) Ordonsky, V. V.; Dros, A.-B.; Schwiedernoch, R.; Khodakov, A. Y. Challenges and Role of Catalysis in CO₂ Conversion to Chemicals and Fuels. *Nanotechnology in Catalysis*; Wiley-VCH Verlag GmbH & Co. KGaA: Weinheim, Germany, 2017; pp 803–850.
- (5) Porosoff, M. D.; Yan, B.; Chen, J. G. Catalytic Reduction of CO₂ by H₂ for Synthesis of CO, Methanol and Hydrocarbons: Challenges and Opportunities. *Energy Environ. Sci.* **2016**, *9* (1), 62–73.
- (6) Posada-Pérez, S.; Ramírez, P. J.; Evans, J.; Viñes, F.; Liu, P.; Illas, F.; Rodriguez, J. A. Highly Active Au/ δ -MoC and Cu/ δ -MoC Catalysts for the Conversion of CO₂: The Metal/C Ratio as a Key Factor Defining Activity, Selectivity, and Stability. *J. Am. Chem. Soc.* **2016**, *138* (26), 8269–8278.
- (7) Ye, R. P.; Ding, J.; Gong, W.; Argyle, M. D.; Zhong, Q.; Wang, Y.; Russell, C. K.; Xu, Z.; Russell, A. G.; Li, Q.; Fan, M.; Yao, Y. G. CO₂ Hydrogenation to High-Value Products via Heterogeneous Catalysis. *Nat. Commun.* **2019**, *10* (1), 5698.
- (8) Navarro-Jaén, S.; Virginie, M.; Bonin, J.; Robert, M.; Wojcieszak, R.; Khodakov, A. Y. Highlights and Challenges in the Selective Reduction of Carbon Dioxide to Methanol. *Nat. Rev. Chem.* **2021**, *5*, 564–579.
- (9) Graciani, J.; Mudiyanse, K.; Xu, F.; Baber, A. E.; Evans, J.; Senanayake, S. D.; Stacchiola, D. J.; Liu, P.; Hrbek, J.; Fernández Sanz, J.; Rodriguez, J. A. Highly Active Copper-Ceria and Copper-Ceria-Titania Catalysts for Methanol Synthesis from CO₂. *Science* (80-). **2014**, *345* (6196), 546–550.
- (10) Rodriguez, J. A.; Liu, P.; Stacchiola, D. J.; Senanayake, S. D.; White, M. G.; Chen, J. G. Hydrogenation of CO₂ to Methanol: Importance of Metal-Oxide and Metal-Carbide Interfaces in the Activation of CO₂. *ACS Catal.* **2015**, *5* (11), 6696–6706.
- (11) Frusteri, F.; Cordaro, M.; Cannilla, C.; Bonura, G. Multifunctionality of Cu-ZnO-ZrO₂/H-ZSM5 Catalysts for the One-Step CO₂-to-DME Hydrogenation Reaction. *Appl. Catal. B Environ.* **2015**, *162*, 57–65.
- (12) Bonura, G.; Cordaro, M.; Cannilla, C.; Mezzapica, A.; Spadaro, L.; Arena, F.; Frusteri, F. Catalytic Behaviour of a Bifunctional System for the One Step Synthesis of DME by CO₂ Hydrogenation. *Catal. Today* **2014**, *228*, 51–57.
- (13) Navarro-Jaén, S.; Virginie, M.; Morin, J.-C.; Thuriot, J. R.; Wojcieszak, R.; Khodakov, A. Hybrid Monometallic and Bimetallic Copper-Palladium Zeolite Catalysts for Direct Synthesis of Dimethyl Ether from CO₂. *New J. Chem.* **2022**, *1* DOI: 10.1039/D1NJ05734K.
- (14) Navarro-Jaén, S.; Virginie, M.; Thuriot-Roukos, J.; Wojcieszak, R.; Khodakov, A. Y. Structure-Performance Correlations in the Hybrid Oxide-Supported Copper-Zinc SAPO-34 Catalysts for Direct Synthesis of Dimethyl Ether from CO₂. *J. Mater. Sci.* **2022**, *57*, 3268–3279.
- (15) Mori, K.; Taga, T.; Yamashita, H. Isolated Single-Atomic Ru Catalyst Bound on a Layered Double Hydroxide for Hydrogenation of CO₂ to Formic Acid. *ACS Catal.* **2017**, *7* (5), 3147–3151.
- (16) Xu, Z.; Mcnamara, N. D.; Neumann, G. T.; Schneider, W. F.; Hicks, J. C. Catalytic Hydrogenation of CO₂ to Formic Acid with Silica-Tethered Iridium Catalysts. *ChemCatChem.* **2013**, *5* (7), 1769–1771.
- (17) Luk, H. T.; Novak, G.; Safonova, O. V.; Siol, S.; Stewart, J. A.; Curulla Ferré, D.; Mondelli, C.; Pérez-Ramírez, J. CO₂-Promoted Catalytic Process Forming Higher Alcohols with Tunable Nature at Record Productivity. *ChemCatChem.* **2020**, *12* (10), 2732–2744.
- (18) Dorner, R. W.; Hardy, D. R.; Williams, F. W.; Willauer, H. D. Heterogeneous Catalytic CO₂ Conversion to Value-Added Hydrocarbons. *Energy Environ. Sci.* **2010**, *3* (7), 884–890.
- (19) Rodemerck, U.; Holéa, M.; Wagner, E.; Smejkal, Q.; Barkschat, A.; Baerns, M. Catalyst Development for CO₂ Hydrogenation to Fuels. *ChemCatChem.* **2013**, *5* (7), 1948–1955.
- (20) Wang, Y.; Gao, W.; Kazumi, S.; Li, H.; Yang, G.; Tsubaki, N. Direct and Oriented Conversion of CO₂ into Value-Added Aromatics. *Chem.-A Eur. J.* **2019**, *25* (20), 5149–5153.
- (21) Li, Z.; Wang, J.; Qu, Y.; Liu, H.; Tang, C.; Miao, S.; Feng, Z.; An, H.; Li, C. Highly Selective Conversion of Carbon Dioxide to Lower Olefins. *ACS Catal.* **2017**, *7* (12), 8544–8548.
- (22) Gao, P.; Dang, S.; Li, S.; Bu, X.; Liu, Z.; Qiu, M.; Yang, C.; Wang, H.; Zhong, L.; Han, Y.; Liu, Q.; Wei, W.; Sun, Y. Direct Production of Lower Olefins from CO₂ Conversion via Bifunctional Catalysis. *ACS Catal.* **2018**, *8* (1), 571–578.
- (23) Li, W.; Wang, H.; Jiang, X.; Zhu, J.; Liu, Z.; Guo, X.; Song, C. A Short Review of Recent Advances in CO₂ Hydrogenation to Hydrocarbons over Heterogeneous Catalysts. *RSC Adv.* **2018**, *8* (14), 7651–7669.
- (24) Ojelade, O. A.; Zaman, S. F. A Review on CO₂ Hydrogenation to Lower Olefins: Understanding the Structure-Property Relationships in Heterogeneous Catalytic Systems. *J. CO₂ Util.* **2021**, *47*, 101506.
- (25) Corma, A.; Melo, F. V.; Sauvanoud, L.; Ortega, F. Light Cracked Naphtha Processing: Controlling Chemistry for Maximum Propylene Production. *Catal. Today* **2005**, *107–108*, 699–706.
- (26) Suganuma, S.; Katada, N. Innovation of Catalytic Technology for Upgrading of Crude Oil in Petroleum Refinery. *Fuel Process. Technol.* **2020**, *208*, 106518.
- (27) Sattler, J. J. H. B.; Ruiz-Martinez, J.; Santillan-Jimenez, E.; Weckhuysen, B. M. Catalytic Dehydrogenation of Light Alkanes on Metals and Metal Oxides. *Chem. Rev.* **2014**, *114* (20), 10613–10653.
- (28) Tian, P.; Wei, Y.; Ye, M.; Liu, Z. Methanol to Olefins (MTO): From Fundamentals to Commercialization. *ACS Catal.* **2015**, *5* (3), 1922–1938.
- (29) Stöcker, M. Methanol-to-Hydrocarbons: Catalytic Materials and Their Behavior. *Microporous Mesoporous Mater.* **1999**, *29* (1–2), 3–48.
- (30) Goud, D.; Gupta, R.; Maligal-Ganesh, R.; Peter, S. C. Review of Catalyst Design and Mechanistic Studies for the Production of Olefins from Anthropogenic CO₂. *ACS Catal.* **2020**, *10* (23), 14258–14282.
- (31) Zhou, W.; Cheng, K.; Kang, J.; Zhou, C.; Subramanian, V.; Zhang, Q.; Wang, Y. New Horizon in C1 Chemistry: Breaking the Selectivity Limitation in Transformation of Syngas and Hydrogenation of CO₂ into Hydrocarbon Chemicals and Fuels. *Chem. Soc. Rev.* **2019**, *48* (12), 3193–3228.
- (32) Zhang, Z.; Yin, H.; Yu, G.; He, S.; Kang, J.; Liu, Z.; Cheng, K.; Zhang, Q.; Wang, Y. Selective Hydrogenation of CO₂ and CO into Olefins over Sodium- and Zinc-Promoted Iron Carbide Catalysts. *J. Catal.* **2021**, *395*, 350–361.

- (33) Ronda-Lloret, M.; Rothenberg, G.; Shiju, N. R. A Critical Look at Direct Catalytic Hydrogenation of Carbon Dioxide to Olefins. *ChemSusChem* **2019**, *12* (17), 3896–3914.
- (34) Liu, R.; Leshchev, D.; Stavitski, E.; Juneau, M.; Agwara, J. N.; Porosoff, M. D. Selective Hydrogenation of CO₂ and CO over Potassium Promoted Co/ZSM-5. *Appl. Catal. B Environ.* **2021**, *284*, 119787.
- (35) Wang, J.; You, Z.; Zhang, Q.; Deng, W.; Wang, Y. Synthesis of Lower Olefins by Hydrogenation of Carbon Dioxide over Supported Iron Catalysts. *Catal. Today* **2013**, *215*, 186–193.
- (36) Zhang, P.; Han, F.; Yan, J.; Qiao, X.; Guan, Q.; Li, W. N-Doped Ordered Mesoporous Carbon (N-OMC) Confined Fe₃O₄-Fe_x Heterojunction for Efficient Conversion of CO₂ to Light Olefins. *Appl. Catal. B Environ.* **2021**, *299* (July), 120639.
- (37) Wu, T.; Lin, J.; Cheng, Y.; Tian, J.; Wang, S.; Xie, S.; Pei, Y.; Yan, S.; Qiao, M.; Xu, H.; Zong, B. Porous Graphene-Confined Fe-K as Highly Efficient Catalyst for CO₂ Direct Hydrogenation to Light Olefins. *ACS Appl. Mater. Interfaces* **2018**, *10* (28), 23439–23443.
- (38) Ramirez, A.; Ould-Chikh, S.; Gevers, L.; Chowdhury, A. D.; Abou-Hamad, E.; Aguilar-Tapia, A.; Hazemann, J.; Wehbe, N.; Al Abdulghani, A. J.; Kozlov, S. M.; Cavallo, L.; Gascon, J. Tandem Conversion of CO₂ to Valuable Hydrocarbons in Highly Concentrated Potassium Iron Catalysts. *ChemCatChem* **2019**, *11* (12), 2879–2886.
- (39) Dorner, R. W.; Hardy, D. R.; Williams, F. W.; Willauer, H. D. K and Mn Doped Iron-Based CO₂ Hydrogenation Catalysts: Detection of KAlH₄ as Part of the Catalyst's Active Phase. *Appl. Catal. A Gen.* **2010**, *373* (1–2), 112–121.
- (40) Wang, X.; Wu, D.; Zhang, J.; Gao, X.; Ma, Q.; Fan, S.; Zhao, T.-S. Highly Selective Conversion of CO₂ to Light Olefins via Fischer–Tropsch Synthesis over Stable Layered K–Fe–Ti Catalysts. *Appl. Catal. A Gen.* **2019**, *573*, 32–40.
- (41) Liu, B.; Geng, S.; Zheng, J.; Jia, X.; Jiang, F.; Liu, X. Unravelling the New Roles of Na and Mn Promoter in CO₂ Hydrogenation over Fe₃O₄-Based Catalysts for Enhanced Selectivity to Light α -Olefins. *ChemCatChem* **2018**, *10* (20), 4718–4732.
- (42) Cheng, Y.; Lin, J.; Wu, T.; Wang, H.; Xie, S.; Pei, Y.; Yan, S.; Qiao, M.; Zong, B. Mg and K Dual-Decorated Fe-on-Reduced Graphene Oxide for Selective Catalyzing CO Hydrogenation to Light Olefins with Mitigated CO₂ Emission and Enhanced Activity. *Appl. Catal. B Environ.* **2017**, *204*, 475–485.
- (43) Visconti, C. G.; Martinelli, M.; Falbo, L.; Infantes-Molina, A.; Lietti, L.; Forzatti, P.; Iaquaniello, G.; Palo, E.; Picutti, B.; Brignoli, F. CO₂ Hydrogenation to Lower Olefins on a High Surface Area K-Promoted Bulk Fe-Catalyst. *Appl. Catal. B Environ.* **2017**, *200*, 530–542.
- (44) Visconti, C. G.; Martinelli, M.; Falbo, L.; Fratalocchi, L.; Lietti, L. CO₂ Hydrogenation to Hydrocarbons over Co and Fe-Based Fischer–Tropsch Catalysts. *Catal. Today* **2016**, *277*, 161–170.
- (45) Zhang, J.; Lu, S.; Su, X.; Fan, S.; Ma, Q.; Zhao, T. Selective Formation of Light Olefins from CO₂ Hydrogenation over Fe–Zn–K Catalysts. *J. CO₂ Util.* **2015**, *12*, 95–100.
- (46) Hu, B.; Frueh, S.; Garces, H. F.; Zhang, L.; Aindow, M.; Brooks, C.; Kreidler, E.; Suib, S. L. Selective Hydrogenation of CO₂ and CO to Useful Light Olefins over Octahedral Molecular Sieve Manganese Oxide Supported Iron Catalysts. *Appl. Catal. B Environ.* **2013**, *132–133*, 54–61.
- (47) Xu, L.; Wang, Q.; Liang, D.; Wang, X.; Lin, L.; Cui, W.; Xu, Y. The Promotions of MnO and K₂O to Fe/Silicalite-2 Catalyst for the Production of Light Alkenes from CO₂ Hydrogenation. *Appl. Catal. A Gen.* **1998**, *173* (1), 19–25.
- (48) Xu, Q.; Xu, X.; Fan, G.; Yang, L.; Li, F. Unveiling the Roles of Fe–Co Interactions over Ternary Spinel-Type ZnCo_xFe_{2–x}O₄ Catalysts for Highly Efficient CO₂ Hydrogenation to Produce Light Olefins. *J. Catal.* **2021**, *400*, 355–366.
- (49) Yuan, F.; Zhang, G.; Zhu, J.; Ding, F.; Zhang, A.; Song, C.; Guo, X. Boosting Light Olefin Selectivity in CO₂ Hydrogenation by Adding Co to Fe Catalysts within Close Proximity. *Catal. Today* **2021**, *371* (August 2020), 142–149.
- (50) Numpilai, T.; Chanlek, N.; Poo-Arpon, Y.; Cheng, C. K.; Siri-Nguan, N.; Sornchamni, T.; Chareonpanich, M.; Kongkachuichay, P.; Yigit, N.; Rupprechter, G.; Limtrakul, J.; Witton, T. Tuning Interactions of Surface-adsorbed Species over Fe-Co/K-Al₂O₃ Catalyst by Different K Contents: Selective CO₂ Hydrogenation to Light Olefins. *ChemCatChem* **2020**, *12* (12), 3306–3320.
- (51) Satthawong, R.; Koizumi, N.; Song, C.; Prasassarakich, P. Light Olefin Synthesis from CO₂ Hydrogenation over K-Promoted Fe–Co Bimetallic Catalysts. *Catal. Today* **2015**, *251*, 34–40.
- (52) Guo, L.; Cui, Y.; Li, H.; Fang, Y.; Prasert, R.; Wu, J.; Yang, G.; Yoneyama, Y.; Tsubaki, N. Selective Formation of Linear-Alpha Olefins (LAOs) by CO₂ Hydrogenation over Bimetallic Fe/Co–Y Catalyst. *Catal. Commun.* **2019**, *130*, 105759.
- (53) Gong, W.; Ye, R.-P.; Ding, J.; Wang, T.; Shi, X.; Russell, C. K.; Tang, J.; Eddings, E. G.; Zhang, Y.; Fan, M. Effect of Copper on Highly Effective Fe–Mn Based Catalysts during Production of Light Olefins via Fischer–Tropsch Process with Low CO₂ Emission. *Appl. Catal. B Environ.* **2020**, *278*, 119302.
- (54) Choi, Y. H.; Jang, Y. J.; Park, H.; Kim, W. Y.; Lee, Y. H.; Choi, S. H.; Lee, J. S. Carbon Dioxide Fischer–Tropsch Synthesis: A New Path to Carbon-Neutral Fuels. *Appl. Catal. B Environ.* **2017**, *202*, 605–610.
- (55) Xu, Y.; Li, X.; Gao, J.; Wang, J.; Ma, G.; Wen, X.; Yang, Y.; Li, Y.; Ding, M. A Hydrophobic FeMn@Si Catalyst Increases Olefins from Syngas by Suppressing C₁ By-Products. *Science* (80-). **2021**, *371* (6529), 610–613.
- (56) Zhao, M.; Yan, C.; Jinchang, S.; Qianwen, Z. Modified Iron Catalyst for Direct Synthesis of Light Olefin from Syngas. *Catal. Today* **2018**, *316*, 142–148.
- (57) Li, S.; Li, A.; Krishnamoorthy, S.; Iglesia, E. Effects of Zn, Cu, and K Promoters on the Structure and on the Reduction, Carburization, and Catalytic Behavior of Iron-Based Fischer–Tropsch Synthesis Catalysts. *Catal. Lett.* **2001**, *77* (4), 197–205.
- (58) Gnanamani, M. K.; Hamdeh, H. H.; Shafer, W. D.; Hopps, S. D.; Davis, B. H. Hydrogenation of Carbon Dioxide over Iron Carbide Prepared from Alkali Metal Promoted Iron Oxalate. *Appl. Catal. A Gen.* **2018**, *564*, 243–249.
- (59) Shafer, W. D.; Jacobs, G.; Graham, U. M.; Hamdeh, H. H.; Davis, B. H. Increased CO₂ Hydrogenation to Liquid Products Using Promoted Iron Catalysts. *J. Catal.* **2019**, *369*, 239–248.
- (60) Ordonsky, V. V.; Luo, Y.; Gu, B.; Carvalho, A.; Chernavskii, P. A.; Cheng, K.; Khodakov, A. Y. Soldering of Iron Catalysts for Direct Synthesis of Light Olefins from Syngas under Mild Reaction Conditions. *ACS Catal.* **2017**, *7* (10), 6445–6452.
- (61) Peron, D. V.; Barrios, A. J.; Taschin, A.; Dugulan, I.; Marini, C.; Gorni, G.; Moldovan, S.; Koneti, S.; Wojcieszak, R.; Thybaut, J. W.; Virginie, M.; Khodakov, A. Y. Active Phases for High Temperature Fischer–Tropsch Synthesis in the Silica Supported Iron Catalysts Promoted with Antimony and Tin. *Appl. Catal. B Environ.* **2021**, *292*, 120141.
- (62) Gu, B.; Peron, D. V.; Barrios, A. J.; Bahri, M.; Ersen, O.; Vorokhta, M.; Šmíd, B.; Banerjee, D.; Virginie, M.; Marceau, E.; Wojcieszak, R.; Ordonsky, V. V.; Khodakov, A. Y. Mobility and Versatility of the Liquid Bismuth Promoter in the Working Iron Catalysts for Light Olefin Synthesis from Syngas. *Chem. Sci.* **2020**, *11* (24), 6167–6182.
- (63) Farrusseng, D. High-Throughput Heterogeneous Catalysis. *Surf. Sci. Rep.* **2008**, *63* (11), 487–513.
- (64) Senkan, S. Combinatorial Heterogeneous Catalysis—A New Path in an Old Field. *Angew. Chemie Int. Ed.* **2001**, *40* (2), 312–329.
- (65) Senkan, S. M. High-Throughput Screening of Solid-State Catalyst Libraries. *Nature* **1998**, *394* (6691), 350–353.
- (66) Paul, S.; Heyte, S.; Katryniok, B.; Garcia-Sancho, C.; Maireles-Torres, P.; Dumeignil, F. REALCAT: A New Platform to Bring Catalysis to the Lightspeed. *Oil Gas Sci. Technol. – Rev. d'IFP Energies Nouv.* **2015**, *70* (3), 455–462.
- (67) Barrios, A. J.; Gu, B.; Luo, Y.; Peron, D. V.; Chernavskii, P. A.; Virginie, M.; Wojcieszak, R.; Thybaut, J. W.; Ordonsky, V. V.; Khodakov, A. Y.; Zelinsky, N. D. Identification of Efficient Promoters

and Selectivity Trends in High Temperature Fischer–Tropsch Synthesis over Supported Iron Catalysts. *Appl. Catal. B Environ.* **2020**, *273*, 119028.

(68) Klencsár, Z. Mössbauer Spectrum Analysis by Evolution Algorithm. *Nucl. Instruments Methods Phys. Res. Sect. B Beam Interact. with Mater. Atoms* **1997**, *129* (4), 527–533.

(69) Wezendonk, T. A.; Santos, V. P.; Nasalevich, M. A.; Warringa, Q. S. E.; Dugulan, A. I.; Chojecki, A.; Koeken, A. C. J.; Ruitenbeek, M.; Meima, G.; Islam, H. U.; Sankar, G.; Makkee, M.; Kapteijn, F.; Gascon, J. Elucidating the Nature of Fe Species during Pyrolysis of the Fe-BTC MOF into Highly Active and Stable Fischer–Tropsch Catalysts. *ACS Catal.* **2016**, *6* (5), 3236–3247.

(70) Torres Galvis, H. M.; Bitter, J. H.; Davidian, T.; Ruitenbeek, M.; Dugulan, A. I.; de Jong, K. P. Iron Particle Size Effects for Direct Production of Lower Olefins from Synthesis Gas. *J. Am. Chem. Soc.* **2012**, *134* (39), 16207–16215.

(71) Wang, S.; Zhai, Y.; Li, X.; Li, Y.; Wang, K. Coprecipitation Synthesis of MgO-Doped ZrO₂ Nano Powder. *J. Am. Ceram. Soc.* **2006**, *89* (11), 3577–3581.

(72) Gusain, D.; Singh, P. K.; Sharma, Y. C. Kinetic and Equilibrium Modelling of Adsorption of Cadmium on Nano Crystalline Zirconia Using Response Surface Methodology. *Environ. Nanotechnology, Monit. Manag.* **2016**, *6*, 99–107.

(73) Su, C.; Li, J.; He, D.; Cheng, Z.; Zhu, Q. Synthesis of Isobutene from Synthesis Gas over Nanosize Zirconia Catalysts. *Appl. Catal. A Gen.* **2000**, *202* (1), 81–89.

(74) Zhang, Z.; Zhang, L.; Hülsey, M. J.; Yan, N. Zirconia Phase Effect in Pd/ZrO₂ Catalyzed CO₂ Hydrogenation into Formate. *Mol. Catal.* **2019**, *475*, 110461.

(75) Chernavskii, P. A.; Kazak, V. O.; Pankina, G. V.; Perfiliev, Y. D.; Li, T.; Virginie, M.; Khodakov, A. Y. Influence of Copper and Potassium on the Structure and Carbidisation of Supported Iron Catalysts for Fischer–Tropsch Synthesis. *Catal. Sci. Technol.* **2017**, *7* (11), 2325–2334.

(76) Subramanian, V.; Ordonsky, V. V.; Legras, B.; Cheng, K.; Cordier, C.; Chernavskii, P. A.; Khodakov, A. Y. Design of Iron Catalysts Supported on Carbon-Silica Composites with Enhanced Catalytic Performance in High-Temperature Fischer–Tropsch Synthesis. *Catal. Sci. Technol.* **2016**, *6* (13), 4953–4961.

(77) Mai, K.; Elder, T.; Groom, L. H.; Spivey, J. J. Fe-Based Fischer–Tropsch Synthesis of Biomass-Derived Syngas: Effect of Synthesis Method. *Catal. Commun.* **2015**, *65*, 76–80.

(78) Yu, G.; Sun, B.; Pei, Y.; Xie, S.; Yan, S.; Qiao, M.; Fan, K.; Zhang, X.; Zong, B. Fe x O y @C Spheres as an Excellent Catalyst for Fischer–Tropsch Synthesis. *J. Am. Chem. Soc.* **2010**, *132* (3), 935–937.

(79) Beasley, C.; Gnanamani, M. K.; Hamdeh, H. H.; Martinelli, M.; Davis, B. H. Effect of Gallium Additions on Reduction, Carburization and Fischer–Tropsch Activity of Iron Catalysts. *Catal. Lett.* **2018**, *148* (7), 1920–1928.

(80) Fellenberg, A. K.; Addad, A.; Hong, J.; Simon, P.; Kosto, Y.; Šmíd, B.; Ji, G.; Khodakov, A. Y. Iron and Copper Nanoparticles inside and Outside Carbon Nanotubes: Nanoconfinement, Migration, Interaction and Catalytic Performance in Fischer–Tropsch Synthesis. *J. Catal.* **2021**, *404*, 306–323.

(81) Ding, J.; Huang, L.; Gong, W.; Fan, M.; Zhong, Q.; Russell, A. G.; Gu, H.; Zhang, H.; Zhang, Y.; Ye, R. Ping CO₂ Hydrogenation to Light Olefins with High-Performance Fe_{0.30}Co_{0.15}Zr_{0.45}-K_{0.10}O_{1.63}. *J. Catal.* **2019**, *377*, 224–232.

(82) Dwyer, D.; Somorjai, G. A. The Role of Readsorption in Determining the Product Distribution during CO Hydrogenation over Fe Single Crystals. *J. Catal.* **1979**, *56* (2), 249–257.

(83) Schulz, H.; Claeys, M. Kinetic Modelling of Fischer–Tropsch Product Distributions. *Appl. Catal. A Gen.* **1999**, *186* (1–2), 91–107.

(84) Yang, J.; Ma, W.; Chen, D.; Holmen, A.; Davis, B. H. Fischer–Tropsch Synthesis: A Review of the Effect of CO Conversion on Methane Selectivity. *Appl. Catal. A Gen.* **2014**, *470*, 250–260.

(85) Govender, N. S.; Botes, F. G.; de Croon, M. H. J. M.; Schouten, J. C. Mechanistic Pathway for C₂₊ Hydrocarbons over an Fe/K Catalyst. *J. Catal.* **2014**, *312*, 98–107.

(86) Olewski, T.; Todici, B.; Nowicki, L.; Nikacevic, N.; Bukur, D. B. Hydrocarbon Selectivity Models for Iron-Based Fischer–Tropsch Catalyst. *Chem. Eng. Res. Des.* **2015**, *95*, 1–11.

(87) Puga, A. V. On the Nature of Active Phases and Sites in CO and CO₂ Hydrogenation Catalysts. *Catal. Sci. Technol.* **2018**, *8* (22), 5681–5707.

(88) Gu, B.; Ordonsky, V. V.; Bahri, M.; Ersen, O.; Chernavskii, P. A.; Filimonov, D.; Khodakov, A. Y. Effects of the Promotion with Bismuth and Lead on Direct Synthesis of Light Olefins from Syngas over Carbon Nanotube Supported Iron Catalysts. *Appl. Catal. B Environ.* **2018**, *234*, 153–166.